JGR Oceans

RESEARCH ARTICLE
10.1029/2023JC019738

In Situ Observations of the Small-Scale Dynamics at Camarinal Sill—Strait of Gibraltar

Jean-Baptiste Roustan[1,2], Lucie Bordois[3], Franck Dumas[3], Francis Auclair[4], and Xavier Carton[1]

[1]University Brest, CNRS, Ifremer, IRD, Laboratoire d'Océanographie Physique et Spatiale (LOPS), IUEM, Plouzané, France, [2]Direction Générale de l'Armement, Ministère des Armées, Paris, France, [3]Service Hydrographique et Océanographique de la Marine (SHOM), Brest, France, [4]Laboratoire d'Aérologie (LA), Toulouse, France

Key Points:

- A recent field experiment highlights a series of Hydraulic Jumps during spring tide floods around the main sill of the Strait of Gibraltar
- High frequency observations reveal local hydraulic control during spring tide ebbs generating westward propagating internal solitary waves
- At neap tide, highly turbulent flows develop, forming an intense bottom boundary layer and large overturns on the sill slope

Correspondence to:
J.-B. Roustan,
jean-baptiste.roustan@polytechnique.edu

Citation:
Roustan, J.-B., Bordois, L., Dumas, F., Auclair, F., & Carton, X. (2023). In situ observations of the small-scale dynamics at Camarinal Sill—Strait of Gibraltar. *Journal of Geophysical Research: Oceans*, *128*, e2023JC019738. https://doi.org/10.1029/2023JC019738

Received 11 FEB 2023
Accepted 19 SEP 2023

Author Contributions:
Conceptualization: Jean-Baptiste Roustan, Lucie Bordois
Data curation: Jean-Baptiste Roustan, Lucie Bordois
Formal analysis: Lucie Bordois, Francis Auclair, Xavier Carton
Funding acquisition: Lucie Bordois, Franck Dumas
Investigation: Jean-Baptiste Roustan, Lucie Bordois, Franck Dumas
Methodology: Jean-Baptiste Roustan, Lucie Bordois
Project Administration: Franck Dumas
Resources: Lucie Bordois, Franck Dumas, Xavier Carton
Software: Jean-Baptiste Roustan
Supervision: Lucie Bordois, Franck Dumas, Francis Auclair, Xavier Carton
Validation: Lucie Bordois

Abstract Recently, PROTEVS GIB20 experiment was performed in the Strait of Gibraltar. Part of this experiment was dedicated to observe the high frequency dynamics near Camarinal Sill (CS), considered as a mixing hotspot in the region. Mooring lines equipped with current profilers and temperature/salinity probes provided data which evidence two dynamical regimes depending on the tidal current intensity; in neap tide floods, local internal hydraulic control is never observed over CS while in spring tide, local internal hydraulic control depicts a tide-dependent and spatially variable pattern. In spring tide floods, measurements revealed the development of a hydraulic jump over the sill and its advection on the lee side. Cross sill sections with CTD casts and acoustic images confirmed this dynamics and depicted a well developed hydraulic jump on the eastern flank of the sill during spring tide ebbs. The north-south and temporal variability of the internal hydraulics was analyzed from several zonal sections over CS, the mean topographic feature of the Strait of Gibraltar. We highlighted a complex series of local hydraulic jumps constrained by topography and a significant north-south variability. The spatiotemporal variability of local hydraulics questions the two dimensional representation of the exchange flow in the Strait of Gibraltar. During neap tide flood, the dynamics of the Mediterranean outflow was investigated from a fixed station. We imaged the development of instabilities at the interface between Atlantic and Mediterranean waters jointly with the generation of much thicker billows deeper. Finally, we discuss our findings in relation to other straits dynamics.

Plain Language Summary A recent field experiment, PROTEVS GIB20, was performed in the Strait of Gibraltar in October 2020. This experiment was partly designed to observe the turbulent dynamics of the flow in this region. The Strait of Gibraltar presents an important topographic sill, Camarinal Sill (CS), where the current reaches its maximum value enhancing the turbulent processes. Understanding the processes developed at this place is of crucial importance to better quantify the induced mixing of the Atlantic/Mediterranean water masses along their journey in the Strait. With acoustic, temperature/salinity, and current measurements we analyzed and described the spatio-temporal variability of the turbulent processes as hydraulic jumps, shear instabilities (like Kelvin-Helmholtz billows) and turbulent gravity current. Finally, we tackled the question of the spatiotemporal variability of the flow near CS and demonstrated that it is far from two-dimensional. Neap tide dynamics reveals large instabilities in the Mediterranean Outflow that may induced significant mixing. All these turbulent processes induce significant mixing between Atlantic and Mediterranean waters and thus influence heat and salinity fluxes through the Strait of Gibraltar.

1. Introduction

The Strait of Gibraltar (SoG in the following) is the locus of complex atmospheric and oceanographic processes. Levantes and Ponientes gap winds combined with strong surface currents render navigation in the Strait quite difficult. The SoG is composed of an east-west channel of about 50 km long, 15 km wide, and 900 m of maximum depth (Figure 1), with a main sill west of Tarifa: Camarinal Sill (CS hereafter) with a minimum depth of 200 m (Figure 1). This complex topographic feature acts as a fence cross-strait. Under these rough environmental conditions, several field experiments were conducted to evaluate the dynamics of the exchange flow in the SoG, but they remain sparse and incomplete. Observing oceanic processes in the SoG is still quite challenging due to the rough environmental conditions (strong operational constraints linked to the maritime traffic, very strong tidal and sheared currents, myriad of fishing boats…). In spite of these difficulties, understanding the 3D exchange flow dynamics is crucial as it preconditions the large scale circulation of the North Atlantic Ocean (Jia, 2000; Mauritzen et al., 2001; Özgökmen et al., 2001; Rahmstorf, 1998; Reid, 1979; Volkov & Fu, 2010) as much as the

Writing – original draft: Jean-Baptiste Roustan
Writing – review & editing: Lucie Bordois, Franck Dumas, Francis Auclair, Xavier Carton

global circulation of the Mediterranean Sea (Harzallah et al., 2014; Naranjo et al., 2014; Sannino et al., 2015). The former authors showed that tide-induced mixing in the SoG can impact the deep water formation in the Gulf of Lyon as well as the Levantine Intermediate Water circulation. In the Atlantic basin, the nature of the Mediterranean outflow directly influences the subtropical Atlantic circulation (Jia, 2000) probably up to the Norwegian current (Reid, 1979).

The exchange flow in the SoG is driven by different mechanisms over a wide range of time scales. At interannual to seasonal scales, the density gradient between cold/salty Mediterranean waters and warm/fresh Atlantic water drives the low frequency outflowing of the Mediterranean (Mediterranean outflow) below the inflowing Atlantic (Atlantic jet) waters (Bryden et al., 1994; Lacombe & Richez, 1982). At a subinertial scale, the atmospheric forcing over the western Mediterranean basin contributes to the exchange flow variability (Candela et al., 1989; García-Lafuente et al., 2002; Vargas et al., 2006). Superimposed to this flow, the barotropic tidal current contributes to half of the current intensity at semi-diurnal and diurnal frequencies (Candela et al., 1990; García-Lafuente et al., 1990). The strong current interacts with the rough topography generating internal tide (García-Lafuente et al., 2000; Morozov et al., 2002), shear instabilities (Wesson & Gregg, 1994), hydraulic jumps (Armi & Farmer, 1988) and high amplitude internal solitary waves (Sánchez-Garrido et al., 2008; Watson & Robinson, 1990; Ziegenbein, 1969, 1970). Those processes enhanced the turbulent mixing of the Mediterranean and Atlantic waters along their journey in the SoG and thus impact the exchange flow properties (García-Lafuente et al., 2013; Macias et al., 2006; Wesson & Gregg, 1994). The present paper focuses on the internal high frequency processes driving mixing in the region of CS. Such processes have been observed earlier, we provide a short review of their past observations.

The first series of experiments in the Strait were held in the 1960s. They are described in different studies (Armi & Farmer, 1985; Lacombe & Richez, 1982; Ziegenbein, 1969), highlighting the existence of hydraulic control along the strait. Armi and Farmer (1985) described some features of the small scale dynamics showing that the pynocline oscillates in phase with the tide and that CS is a favorable region for the mixing of Atlantic and Mediterranean waters.

Jointly with the development of the 2D hydraulic control theory to explain the baroclinic flow in the Strait of Gibraltar (Armi & Farmer, 1986), an extensive field experiment—*The Gibraltar Experiment*—with moorings and intensive ship survey was performed between 1985 and 1986 (Kinder & Bryden, 1987). The density driven flow was shown to comply with the hydraulic control theory (Armi & Farmer, 1988); an important modulation of the tidal current was observed especially at CS where the control vanishes during some floods (Violette & Lacombe, 1988). A spectral analysis of the tide showed the predominance of the semi-diurnal component which represented 96% (respectively 74%) of the sea level (resp. current) variance in the strait noticeably influenced by the diurnal variations (Candela et al., 1990; García-Lafuente et al., 1990). Because of the standing-wave pattern of the tide in the strait, the tidal current heads west (flood hereafter) between low and high water and heads east between high and low water (ebb hereafter).

The formation of a hydraulic jump on the west slope of CS was observed during strong floods as predicted by the hydraulic theory (Armi & Farmer, 1986, 1988). When the flow slackens, this hydraulic jump creates an internal bore which propagates eastward over the crest of CS as described by Armi and Farmer (1988). The unstable bore degenerates into a train of high-energy internal solitary waves, which have been widely observed (Alpers et al., 1996; Armi & Farmer, 1988; Watson & Robinson, 1990; Ziegenbein, 1970), described (Gómez-Enri et al., 2007; Sánchez-Garrido et al., 2008; Vásquez et al., 2008) and modeled (Hilt, 2022; Hilt et al., 2020; Morozov et al., 2002; Sánchez-Garrido et al., 2011; Vlasenko et al., 2009).

During the same survey, micro-structure measurements revealed some characteristics of the mixing processes in the SoG. Wesson and Gregg (1994) exhibited maximum turbulent dissipation rate of 10^{-2} W kg^{-1} west of CS which makes it the mixing hotspot in the SoG. Surprisingly, averaged turbulent dissipation rates on the same order of magnitude (around 10^{-4} W kg^{-1}) were found during spring and neap tide floods except for the Atlantic layer west of the Sill. The authors suspected an underestimation of the dissipation rate in their study linked to the incomplete data set in spring tide.

In the beginning of the 21st century, Macias et al. (2006) analyzed the mixing variability over CS through the composition of the water masses, with data from a 2002/2003 cruise. The authors used the percentage of North Atlantic Central Water, the thinnest layer between South Atlantic Water and Mediterranean Water (Gascard &

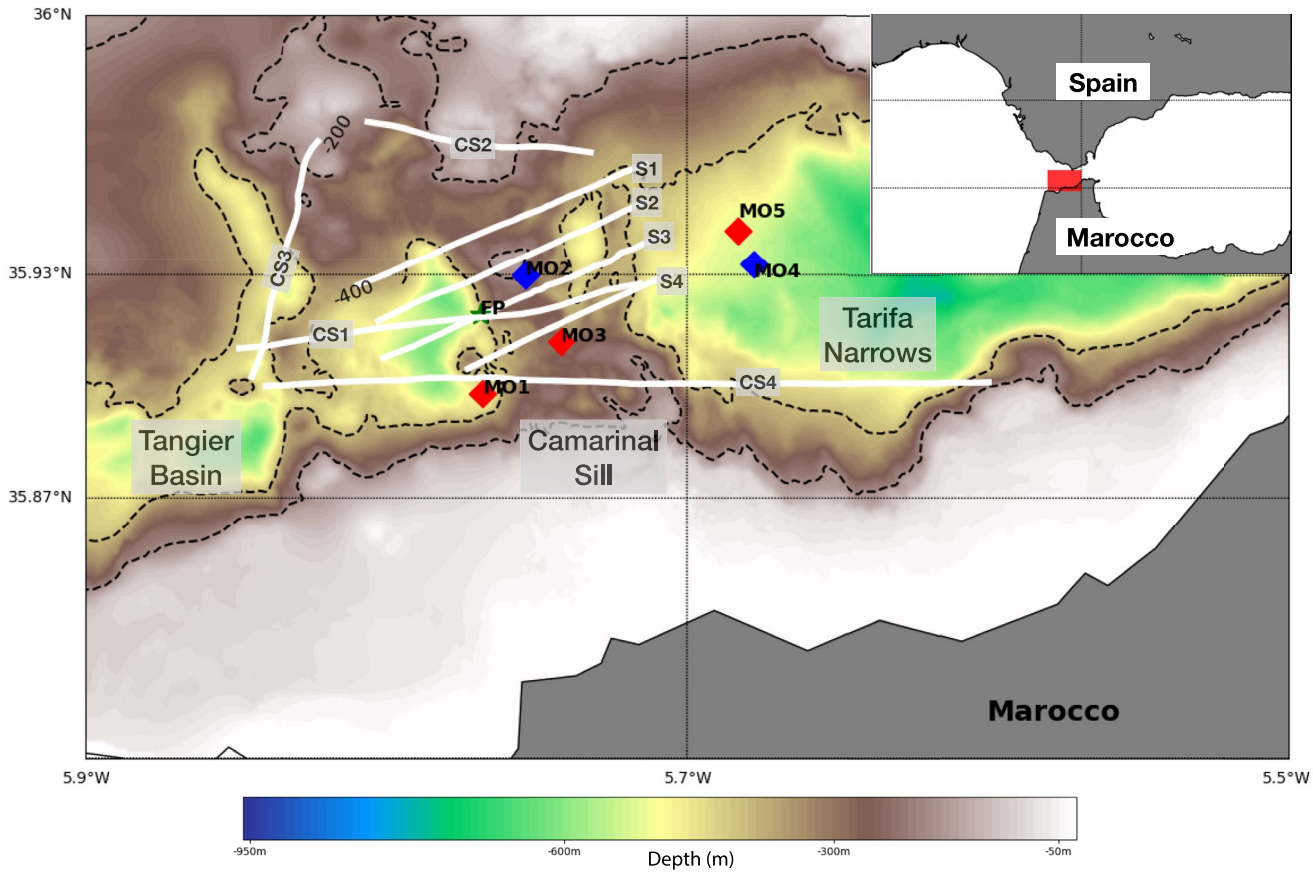

Figure 1. *Inset*: The spatial scope of the PROTEVS GIB20 experiment. The red box is the area analyzed in this paper. *Map*: Bathymetry of the Camarinal Sill region with the position of the hydrologial moorings MO1, MO3, and MO5 (red diamonds) and the current profilers MO2 and MO4 (blue diamonds). Sections S1, S2, S3, S4, CS1, CS2, CS3, and CS4 are printed with white lines. The average position of the station FP is depicted with a green star.

Richez, 1985), as an indicator of the mixing (Gascard & Richez, 1985). The authors highlighted an inverse relationship between the percentage of the North Atlantic Central Water and the tidal amplitude, arguing for stronger mixing during spring tides which causes the erosion of this thin layer.

In the late 1990s, the SECEG survey was conducted over CS during neap tides (Bruno et al., 2002). These measurements showed internal topographic trapped waves over CS, with a different nature from the internal bore created in supercritical conditions over the sill. These waves had previously been observed by Violette and Lacombe (1988) and Richez (1994) with airborne synthetic aperture radar without being able to give an explanation on the nature of their observations. Bruno et al. (2002) demonstrated that these high amplitude internal waves can only be trapped in neap tide, under locally subcritical conditions, enhanced by a resonance mechanism.

More recently, García-Lafuente et al. (2018) addressed the question of the symmetry of the high frequency processes during ebb and flood by analyzing the data of two bottom conductivity-temperature (CT) sensors and Acoustic Doppler Current Profiler (ADCP) mooring lines, north and south of the main crest of CS. The authors found favorable conditions for the formation of a hydraulic jump on the eastern flank of CS during strong ebbs, supporting the first findings of Armi and Farmer (1988). Recent numerical models highlighted the formation of a smaller hydraulic jump on the eastern flank of CS during the ebbs in spring tides (Sánchez-Garrido et al., 2011; Sannino et al., 2004). Westward propagating internal waves west of CS were observed by Alpers et al. (1996). They were associated to perturbations of the seasonal thermocline. García-Lafuente et al. (2018) also reported high frequency variability of the temperature and salinity at the bottom of their northern mooring suggesting the westward propagation of an internal bore. In addition, they mentioned high frequency velocity fluctuations in the southern part of CS during the strongest floods. They hypothesized shear instabilities or a transient upstream hydraulic jump which comply with the approach control theory (Farmer & Denton, 1985). The

upstream hydraulic jump hypothesis is supported by the result of the Sánchez-Garrido et al. (2011) numerical model and by the hyperspectral images described by Navarro et al. (2018).

The wide literature mentioned above provides an extensive description of the high frequency dynamics of the SoG. Nevertheless, the interaction between the exchange flow and these very energetic fine-scale turbulent processes remains poorly understood. Recent advances in numerical modeling show that the flow dynamics is complex and strongly 3D near CS with temporal variability primarily tidally driven (Bordois et al., 2017; Hilt et al., 2020; Sánchez-Garrido et al., 2011; Sannino et al., 2004). Sánchez-Garrido et al. (2011) and more recently Hilt (2022) ran high resolution (50 m horizontally) fully non-hydrostatic models, that reveal the complex 3D structure of the hydraulic control near CS. From the previous field experiment, authors characterized the local internal hydraulics with a 2D along strait vision. The new intensive data set described in this paper allows us to explore the north-south and 3D variability, the temporal variability and the flood-ebb asymmetry of the local internal hydraulics, which are of crucial importance according to the results of the latest fully non-hydrostatic models.

To fill this gap, the PROTEVS GIB20 experiment was conducted in the SoG on the RV *L'Atalante* during October 2020. It consisted in an extensive survey of the Strait with acoustics and conductivity/temperature sensors jointly with five mooring lines near CS. The campaign was designed to address the question of the interaction of the turbulent fine-scale dynamics with the 3D exchange flow in the SoG. The present paper tackles three main questions that remain poorly understood in the literature. First we want to characterize the dynamical regimes that develop near CS. The second point is to assess the impact of the 3D topographic structure of the Sill and temporal variability on hydraulic dynamics. Finally, we investigate the poorly described neap tide dynamics focusing on the instabilities that develop in the Mediterranean outflow. Wesson and Gregg (1994) found, surprisingly, a similar averaged dissipation rate for spring tide and neap tide especially for the Mediterranean waters. We investigate the mechanism capable of generating such mixing in neap tides.

The paper is organized as follows. The first section describes the data used for the analysis. The second section describes briefly the low frequency forcing during the campaign. The third section describes the small-scale, high-frequency processes in the SoG, observed during the GIB20 data and characterize the internal hydraulics of the exchange over CS. Finally, we discuss the new results and their possible impact on the exchange flow.

2. Data

The PROTEVS GIB20 experiment was a large intensive survey in the SoG, the Bay of Cadiz and the Alboran Sea during part of a strong (near equinox) fortnightly cycle in October 2020. This paper focuses on a few measurements performed during the experiment designed to observe the internal high frequency processes at CS. This section presents exclusively the data analyzed in this paper. Hindcast atmospheric data from the Arpege model of Meteo France are also analyzed.

The analyzed data set consists in five moorings designed to sample at very high frequency both hydrological and currents data along the entire water column all around CS. In addition, extensive sections were performed over CS during spring and neap tides. The location of the measurements is presented in Figure 1.

During the campaign the current was continuously measured with the OS 38 and OS 150 kHz VMADCP looking down from the hull of the research vessel. The data were averaged in 1 min frames. In the following, the OS38 kHz data is used to get deeper currents. SIMRAD EK60 echosounder observations were also recorded. The echosounder detects the reflector (suspended particulate matter) distributions, allowing to visualize the stratification of the water column and thus the fine and turbulent structures at the interfaces. This echosounder pings at 3 different frequencies, 200, 38, and 12 kHz. The 38 kHz frequency is used in this study as the best compromise between resolution and range.

2.1. Mooring Lines

During the experiment, three hydrological mooring lines equipped with SBE37 and SBE56 sensors (see Table 1 for details) MO1, MO3, MO5 were deployed (Figure 1). SBE37 probes are temperature, conductivity and pressure recorders; SBE56 sensors measure only temperature. They were deployed along a mooring line from the bottom to about 50 m below the surface. Pressure gauges are essential to correct the current-induced sinking of

Table 1
Description of the Mooring Lines

Moorings	Sensors	Position (lon, lat)	Time laps	Sample frequency (Hz)	Depth at mooring position (m)
MO1	CT and pressure probes: 8 SBE37 + 21 SBE 56	−5.768°W, 35.898°N	2020/10/08 15 hr–2020/11/09 12 hr	SBE37: 10' SBE56: 1'	479
MO2	ADCP CONTINENTAL 190 kHz, pressure and temperature SBE26 probe at the bottom	−5.754°W, 35.930°N	2020/10/08 5 hr–2020/10/17 15 hr	ADCP: 30' SBE26: 60'	192
MO3	CT and pressure probes: 7 SBE37 + 12 SBE 56	−5.742°W, 35.912°N	2020/10/08 13 hr–2020/10/22 21 hr	SBE37: 10' SBE56: 1'	293
MO4	ADCP 75 kHz 40 m above the bottom	−5.678°W, 35.933°N	2020/10/08 7 hr–2020/10/17 14 hr	ADCP: 60'	537
MO5	CT and pressure probes: 11 SBE37	−5.683°W, 35.942°N	2020/10/08 9 hr–2020/11/01 14 hr	SBE37: 10'	529

Note. Time is in UT. The depth at the mooring position comes from the SHOM bathymetry data set.

the instrument during the strong spring tidal flows (up to 200 m). The depth of the SBE56 was assessed from the pressure measurement of the nearest SBE37 with the assumption of a strait line between 2 successive SBE37. Note that all SBE56 were interspersed between two SBE37. Then the Conductivity Temperature (CT) information were interpolated to obtain CT evolution at fixed depths. Note that due to the current-sinking, the depth of the shallowest sensor evolved along the tidal cycle. Therefore, no data were recorded in the Atlantic layer during the strongest tides especially at MO1 and MO3, which are subject to strongest currents. The temporal resolution of the SBE37 (resp. SBE56) was 10 (resp. 1) seconds. To our knowledge, this is the first attempt to collect hydrological information from the bottom to the top of the interfacial mixed layer at such a frequency.

We deployed two current profilers MO2 and MO4 (Figure 1). MO2 was equipped with a CONTINENTAL 190 kHz ADCP looking upward. It was bottom mounted on a frame together with an SBE26 T/P recorder. MO4 was equipped with a 75 kHz RDI ADCP looking upward. They were deployed from the 8 October to the 17 October (see Table 1 for details). These instruments sampled the water column from the bottom (30 m above the ground) up to 37 m (16 m) below the surface for MO2 (MO4) at 30 s (60 s) interval with vertical bins of 5 m (8 m). The standard error of the 75 kHz RDI instrument is ±4.32 cm/s for both horizontal and vertical speeds (constructor communication). This value corresponds to an upper bound especially for the vertical speed which is derived from the four beam data (rather than two for each component of horizontal speed) of the instrument and is less impacted by the projection errors as the beams are near vertical (20° tilted). The barotropic current ($\bar{U}$, $\bar{V}$) was computed from these ADCP observations as the vertically averaged current at each time step filtered with a 1 hr running-average. This methodology slightly underestimates the contribution of the upper layer (and the bottom layer for MO4) in the barotropic current as no data were recorded in the shallowest few tens of meters.

2.2. Sections

To observe the spatial variability over the sill, successive sections of about 10 km were performed along the direction perpendicular to the isobaths during both neap and spring tides. These four typical sections are named S1, S2, S3, and S4 from North to South (Figure 1); each of them was performed at least once during neap tide (the 10 October) and spring tide (between the 17 and 18 October). Details are given in Table 2. During the sections, a Moving Vessel Profiler (MVP), equipped with CTD sensors, was towed behind the vessel traveling at around 4 knots. The use of the MVP allowed an extensive and fast sampling suitable for fine, rapidly evolving processes. Four other sections CS1, CS2, CS3, CS4, performed during one spring tide flood are also analyzed.

2.3. Station

A 5-hr station performed on the western slope of CS, is analyzed in this paper (FP in Figure 1). This station was performed during ebb on the 11 October afternoon. Three CTD casts were performed during this station. The objective was to observe the rapid evolution of the Mediterranean outflow above the steep western slope of CS where mooring lines cannot be deployed. Note that our CTD was equipped with a pair of CT sensors mounted at the bottom and the top of the frame, which allows us to analyze the upward profile.

3. Low Frequency Forcing During PROTEVS GIB20 Experiment

Small-scale processes in the SoG are mainly forced by strong gap winds, barotropic tides (Candela et al., 1990; García-Lafuente et al., 1990; Sánchez-Garrido et al., 2011), atmospheric pressure gradient (Candela et al., 1989) and the long-term density-driven baroclinic flows which is composed of the Atlantic Jet flowing over the Mediterranean Outflow (Lacombe & Richez, 1982). In this section, we briefly describe these forcings during the PROTEVS GIB20 experiment. Note that the wind plays a crucial role for the surface currents and the internal seasonal thermocline dynamics (Peliz et al., 2009). However this paper focuses on the internal dynamics at the interfacial mixed layer (halocline at ≈150 m depth (Candela et al., 1989)) which is not directly impacted by the wind.

Table 2
Description of the Sections

Sections	Instruments	Time laps	Tide phase	Tidal current direction
Spring tides				
S4_1ST	MVP + EK60 + VMADCP	2020/10/17 17:26–2020/10/17 18:04	LW − 2	Ebb (eastward)
S1_1ST	MVP + EK60 + VMADCP	2020/10/17 19:04–2020/10/17 20:37	LW	Flow inversion
S3_ST	MVP + EK60 + VMADCP	2020/10/17 21:02–2020/10/17 23:02	LW + 2	Flood (westward)
S2_ST	MVP + EK60 + VMADCP	2020/10/17 23:18–2020/10/18 00:04	LW + 4	Flood (westward)
S4_2ST	MVP + EK60 + VMADCP	2020/10/18 00:27–2020/10/17 02:35	LW + 5	Flood (westward)
CS1	MVP + EK60 + VMADCP	2020/10/17 11:02–2020/10/17 13:42	LW + 3/4/5	Flood (westward)
CS2	MVP + EK60 + VMADCP	2020/10/19 11:34–2020/10/19 12:04	LW + 2	Flood (westward)
CS3	MVP + EK60 + VMADCP	2020/10/19 12:12–2020/10/19 13:18	LW + 3	Flood (westward)
CS4	MVP + EK60 + VMADCP	2020/10/19 13:26–2020/10/19 16:42	LW + 4/5	Flood (westward)
Neap tides				
S2_1NT	MVP + EK60 + VMADCP	2020/10/10 12:42–2020/10/10 13:16	LW − 2	Ebb (eastward)
S4_NT	MVP + EK60 + VMADCP	2020/10/10 15:15–2020/10/10 16:38	LW + 2	Flood (westward)
S2_2NT	MVP + EK60 + VMADCP	2020/10/10 16:54–2020/10/10 18:05	LW + 4	Flood (westward)
S3_NT	MVP + EK60 + VMADCP	2020/10/10 18:23–2020/10/10 19:35	LW + 5	Flood (westward)

Note. Time is in UT. LW is for low water at Tarifa.

The barotropic flow in the SoG $(\bar{U})$, computed as a vertically averaged zonal current filtered with a 1 hr running-average, varies from 1 up to 2 m/s between neap and spring tides over CS (blue curve Figure 2a). This value decreases by half in deeper areas as at MO4 (orange curve in Figure 2a). Throughout the fortnightly cycle, this flow corresponds to really high Reynolds numbers (Re $\approx 10^9$ for a typical length of 10 km and $\nu = 10^{-6}$ m^2 s^{-1}) where many energetic turbulent processes occur.

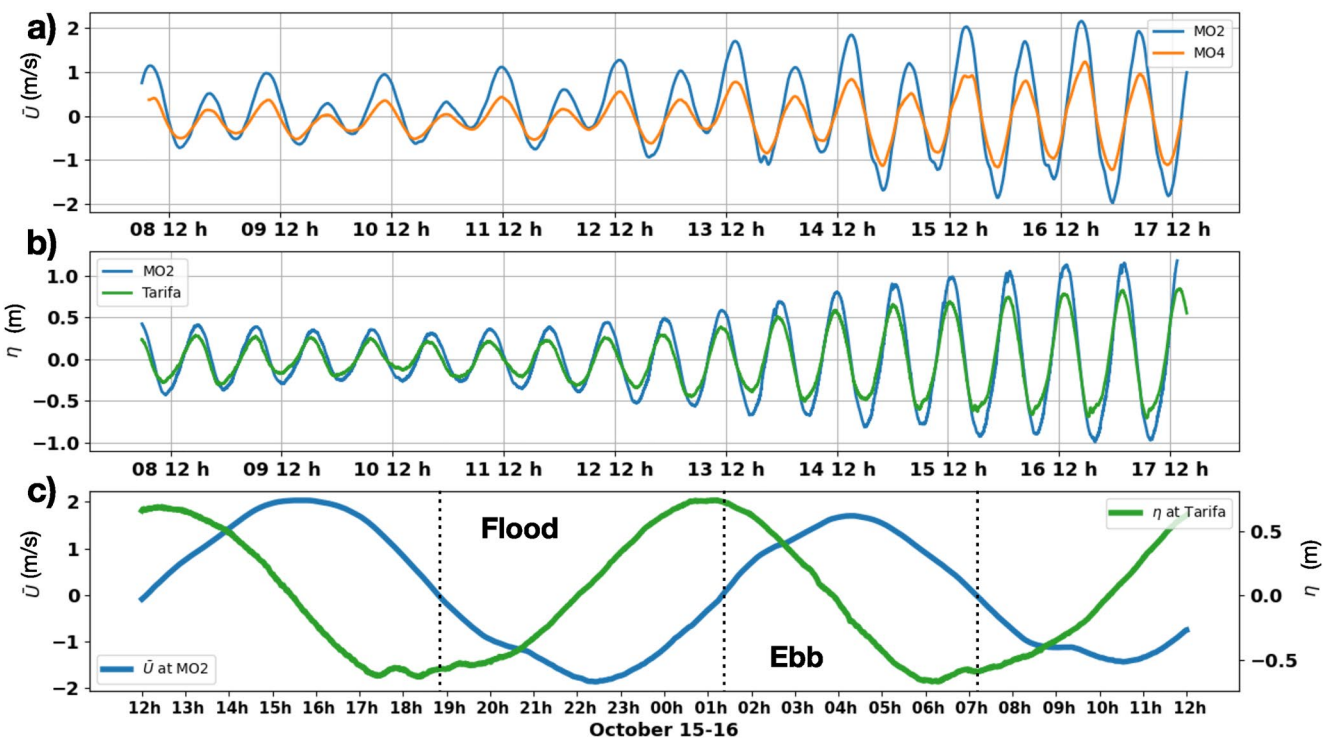

Figure 2. Characterization of the tide near Camarinal Sill: (a) Barotropic current at MO2 (blue curve) and MO4 (orange curve), (b) sea level oscillation at MO2 (blue curve) and Tarifa tide gauge (green curve), (c) sea level oscillation at Tarifa tide gauge (green curve) and barotropic current at MO2 (blue curve) zoomed between the 15 October 12:00 and the 16 October 12:00.

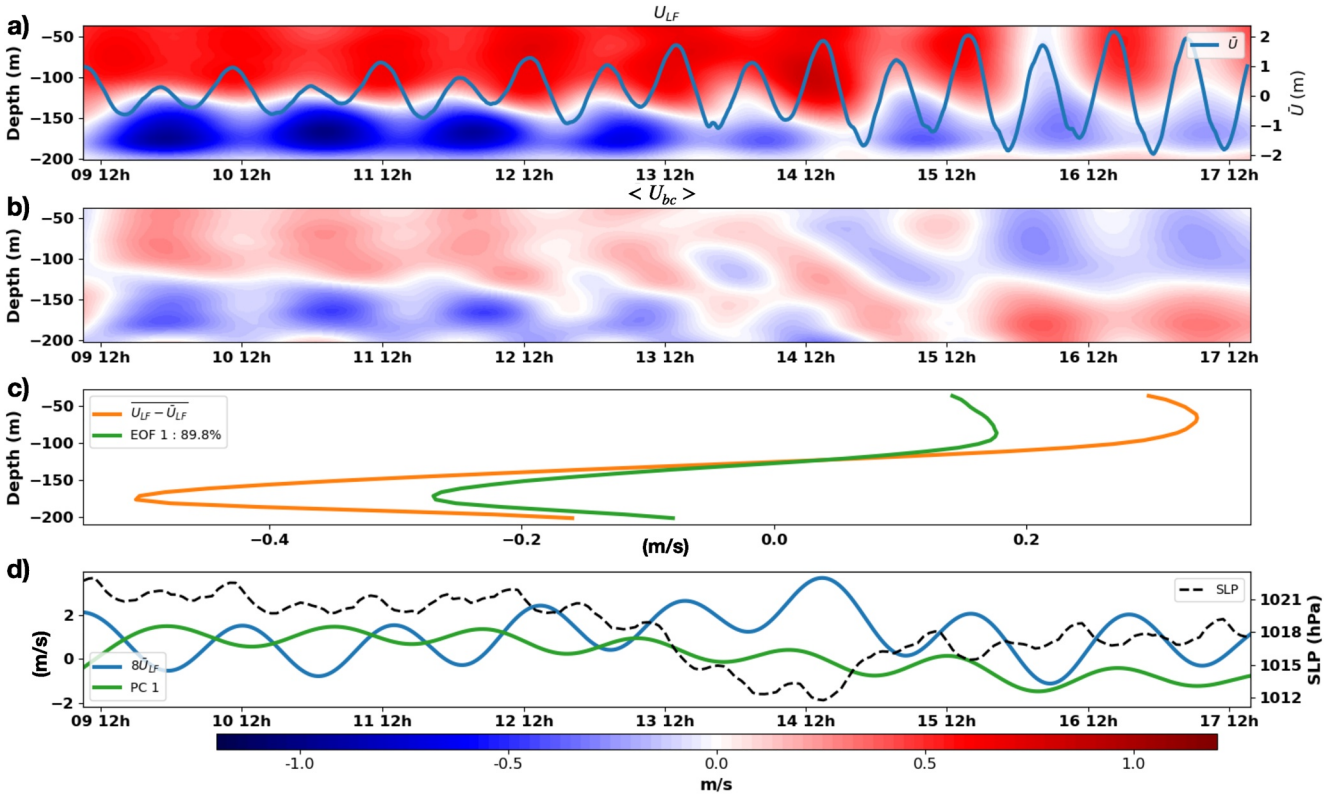

Figure 3. Low frequency zonal flow at Camarinal Sill (MO2 mooring): (a) Low pass filtered (1/28 cph) zonal flow U_{LF}. Blue curve is the barotropic flow superimposed. (b) The low pass centered baroclinic zonal current $U_{LF} - \bar{U}_{LF} - \overline{U_{LF} - \bar{U}_{LF}}$ noted $<U_{bc}>$ (see text for details) (c) First Empirical Orthogonal Function (EOF) of $<U_{bc}>$ (green curve) and the temporal average of the low pass baroclinic zonal current $\overline{U_{LF} - \bar{U}_{LF}}$ (orange curve). (d) Time coefficient evolution of the first EOF mode (green curve) and height time the low pass barotropic zonal current $\bar{U}_{LF}$ (blue curve). The black dashed curve is the sea level pressure from the Arpege Meteo France reanalysis averaged over the western Mediterranean basin.

Interestingly, the sea level over the sill (in MO2) is almost in phase (delayed by a couple of minutes) with the sea level at Tarifa (Figure 2b). In addition, the barotropic flow at MO2 heads east (tidal inflow) during the ebb and heads west (tidal outflow) during the flood (Figure 2c) which is due to the standing wave nature of the tide in the SoG (García-Lafuente et al., 1990). In the following, ebb refers to eastward tidal current (tidal inflow) and flood to westward tidal current (tidal outflow).

The low frequency zonal flow U_{LF} was computed from the ADCP data at MO2 with a 8th order butterworth low pass filter at cutting period of 28 hr. This method follows Vargas et al. (2006), except that we use a low-pass filter rather than a band-pass filter in order to keep long-term and subinertial contributions together. We removed the vertically averaged component of the signal (low frequency barotropic zonal current $\overline{U_{LF}}$) to obtain the baroclinic low frequency zonal current ($U_{LF,bc}$). To enhance the variance analysis, the depth-dependant temporal-averaged was removed from the $U_{LF,bc}$ to get the centered low pass baroclinic zonal current ($<U_{bc}>$ in the following). Note that the analysis focuses on the zonal current, considered as the dominant part of the exchange flow in the SoG. Then, $<U_{bc}>$ was decomposed with an Empirical Orthogonal Function (EOF) tool based on singular value decomposition.

Figure 3 presents (a) the low frequency zonal flow U_{LF}, (b) $<U_{bc}>$ time series, (c) the temporally averaged profile of $U_{LF,bc}$ (orange curve) with the first EOF mode (green curve) explaining 90% of the variance of $<U_{bc}>$, (d) the first EOF mode time-coefficient (green curve) superimposed with the evolution of the Sea Level Pressure (SLP) averaged over the western Mediterranean basin (black dashed curve from the METEO FRANCE Arpege reanalysis) and the low frequency barotropic zonal flow $\overline{U_{LF}}$ (blue curve). The analysis starts on the 9 October at midday to avoid the first day polluted by the filtering process.

The low frequency circulation is widely baroclinic, a component which represents about 70% of the total low frequency current. It is composed of two layers flowing in opposite directions, the eastward Atlantic jet and westward Mediterranean outflow flowing at about 0.5 m/s (Figures 3a and 3c), with 0.12 m/s (30%) of barotropic contribution on average (time average of the blue curve Figure 3d). Therefore, this exchange is dominated by the long term density-driven baroclinic circulation between the Atlantic and Mediterranean waters (Lacombe & Richez, 1982). However, this baroclinic flow presents some variability during the studied period mainly due to a modulation of the shear as the baroclinic shape of the first EOF mode indicates. The time coefficient of the first EOF shows an inversion between neap to spring tide (green curve Figure 3d going from 2 to −2), which indicates a decrease of about 80% of the low frequency baroclinic flow.

The baroclinic flow is inversely proportional to the tidal strength which corresponds to the fortnightly oscillation of the subinertial current due to the modulation of tidal mixing (Candela et al., 1989; Vargas, 2004; Vargas et al., 2006). According to the former authors, this modulation is due to the tidal mixing enhanced in spring tide. This increases the turbulent viscosity in spring tide, and limits the shear between both layers. This explains the reduction of the baroclinic component of the flow highlighted by the inversion of the time coefficient of first EOF mode. The 1 day modulation of the first EOF coefficient supports the previous explanation as a marker of the diurnal oscillation of the tidal strength. We observe minimum/maximum absolute values of the first EOF coefficient at the diurnal maximum/minimum tide. Note that long-term density variations might influence the low frequency barotropic current, but over such short period that they are unlikely to explain the observed variability.

The barotropic low frequency flow is strongly affected by the atmospheric pressure over the western Mediterranean Sea. We observe an anti-correlation between this signal and the SLP over the Mediterranean Sea (Figure 3d). It suggests that the barotropic low frequency flow corresponds to a subinertial flow widely enhanced by atmospheric conditions over the Mediterranean basin (Candela et al., 1989; García-Lafuente et al., 2002; Vargas et al., 2006). The Candela et al. (1989) model shows that the subinertial barotropic flow in the SoG responds as an inverse barometer of the integrated atmospheric pressure over the entire Mediterranean basin. The barotropic low frequency flow also presents diurnal fluctuations; that are likely due to diurnal tidal variations remaining in the low frequency signal filtered with a 28 hr cutoff period.

In summary, we described the variability of the low frequency currents around CS during PROTEVS GIB20 experiment. The exchange flow at CS is significantly modulated by the fortnightly tidal cycle. The low frequency variability of the barotropic current is highly correlated with the atmospheric conditions over the western Mediterranean Basin. Consequently, the strength of the observed barotropic flow at CS is modulated by long term density variations (not shown here), remote atmospheric-driven barotropic flow and fortnightly variations of the tidal barotropic currents.

4. Camarinal Sill Dynamics

This section addresses the mains issues discussed in this paper. We first introduce the hydraulic theory before analyzing the different regimes that dominate the flow at CS. Since they appear to be constrained by the tidal strength, we investigate in detail first the spring tide and then the neap tide dynamics.

4.1. Hydraulic Theory

A large part of the exchange flow theory in the SoG is based on the hydraulic control theory in the two layers approximation. The flow can be separated in three hydraulic states: subcritical, critical, and supercritical, depending on whether the long waves are able to propagate in both directions. A hydraulic transition from subcritical to supercritical flow is associated with much instability usually related to a plunge of the isopycnals. The transition from supercritical to subcritical triggers a hydraulic jump (see Figure 5 of Sánchez-Garrido and Nadal (2022)). The distinction between these states is based on the Froude number F, generally computed as the local composite Froude number $G^2 = F_1^2 + F_2^2$ where $F_i^2 = U_i^2/(g'h_i)$, with i stands for layers 1 and 2 and g' the reduced gravity defined as $g(\rho_2 - \rho_1)/\bar{\rho}$, ρ_i the density of layer i and $\bar{\rho}$ the averaged density. The local composite Froude number gives information on the local criticality of the flow, and mathematically $G^2 > 1$ is necessary for the development of stationary disturbances like hydraulic jumps (see Appendix 1 of Sánchez-Garrido et al. (2011) for more mathematics details). However, hydraulic control

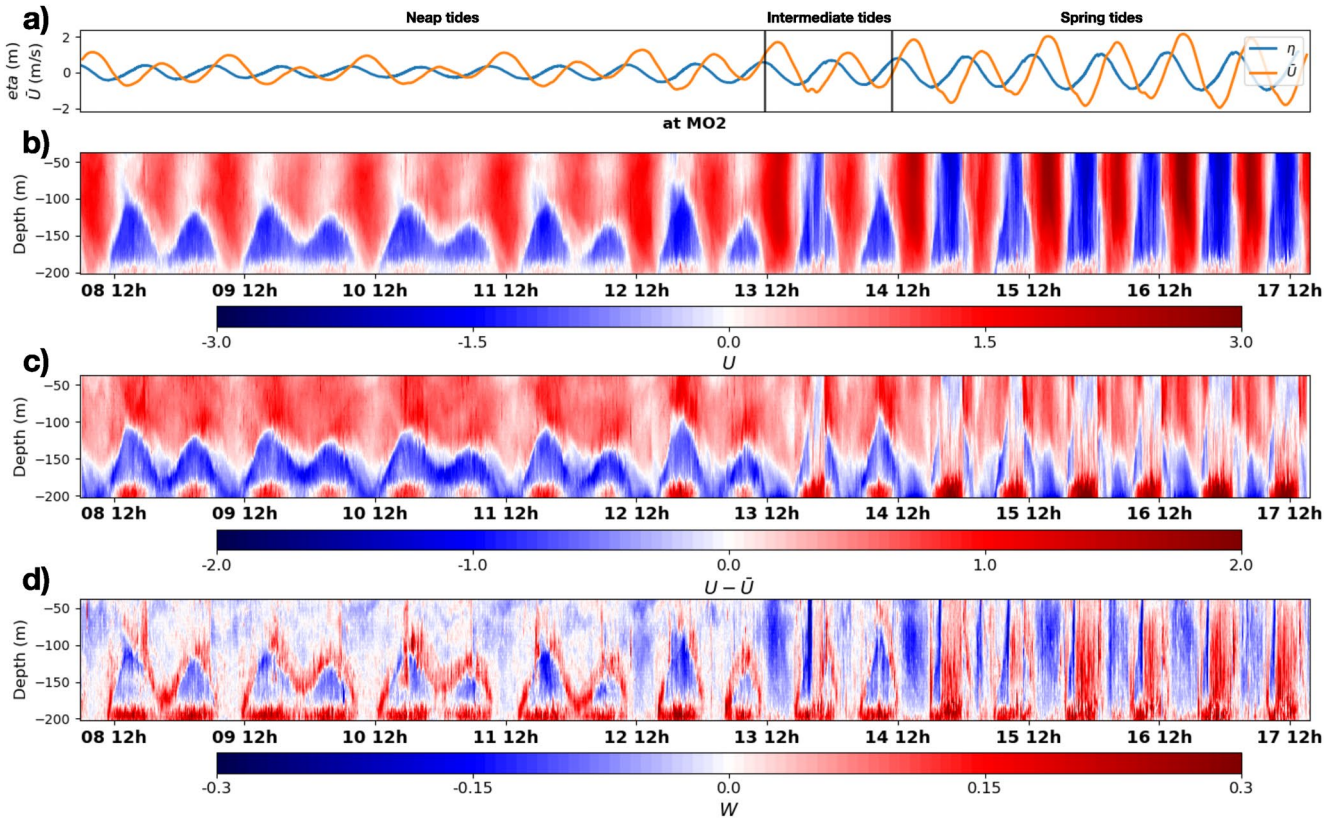

Figure 4. (a) Sea level (blue curve) and barotropic current (orange curve) at MO2. Neap tide period extends from 8th to the 13th midday, spring tide period from the 14th midday to the 17th. The period in between is considered as intermediate tide. (b) Zonal current at MO2 from the 8 October 2020 to the 17 October 2020. (c) Same as (b) for the zonal baroclinic current computed as the total zonal current minus its vertical average at each time step. (d) Same as (b) for the vertical velocity.

of a cross-strait section is not guaranteed by $G^2 > 1$. Pratt (2008) developed a criterion for (global) hydraulic control, based on the cross-strait integration of the local composite Froude number. Even if our data set covers 4 distinct along strait sections (S1 to S4), integrating non-instantaneous data could be tricky in this fast-changing environment. Therefore, the following analysis remains local and refers to the ability for local disturbances to develop.

The choice of the 2D composite Froude number remains open to criticism as many studies show the importance of the mixed layer in the exchange flow dynamics (Bray et al., 1995; Sannino et al., 2007). However, the mathematical meaning of the composite Froude number in terms of local instability (Appendix 1 of Sánchez-Garrido et al. (2011)) is helpful to discuss the local criticality of the flow. Moreover, this definition, which is similar to the one used in the pioneering study by Armi and Farmer (1988), facilitates the comparisons with the literature. In Appendix A, we compare different computations of Froude numbers and discuss the limitations of each approach.

The calculation of the composite Froude number requires to define two layers. We used the isohaline at 37.2 psu which corresponds to the interface in salinity between Mediterranean and Atlantic waters near CS (Bray et al., 1995). Knowing the depth of the interface, we computed the averaged speed and density in both layer to obtain the composite Froude number.

4.2. Dynamical Regimes

The 3D current profiles at MO2 present two distinct patterns following the magnitude of the tidal current, one during the neap tides and a quite different one during spring tides illustrating different dynamics. Figure 4 presents ADCP measurements of the (a) barotropic, (b) total, (c) baroclinic zonal current, and (d) vertical velocity at MO2 from the 8 to the 17 October. It clearly exhibits differences for both the zonal current (U) and the vertical velocity (W) along the fortnightly cycle.

Indeed, the observation period covers part of a fortnightly cycle, with neap tides from the 8 (beginning of MO2 observations) to the 13 October and spring tides from the 14 to the 17 October (end of MO2 observations). The period between the two is considered as intermediate tides. During the neap tides, the flow remains largely baroclinic, with the Atlantic flowing eastward on the deeper Mediterranean outflow (Figure 4b). The depth of the interface between both layers - defined as the zero of the total zonal (U) current when no CT data are available—fluctuates around 150 m depth, diving during the ebb. The influence of the diurnal amplification of the tidal current is visible, with the interface reaching the bottom once a day at the peak of the maximum ebb. However, the baroclinic structure is maintained while removing the barotropic tidal component (Figure 4c).

During the spring tides the flow is much more barotropic with a characteristic alternation between eastward and westward flow respectively during ebbs/floods (Figure 4b). The baroclinic flow presents high frequency variations such that the Atlantic and Mediterranean layers are no longer distinguishable above the sill (Figure 4c). This dynamics will be detailed later.

The dynamical regimes create different signatures in the vertical velocity profile (Figure 4d). During neap tides the variations of the vertical velocity (W) profiles are slowly varying, with a strong vertical gradient at the interface between Atlantic and Mediterranean waters during floods (Figure 4d). This pattern suggests shear instabilities development along the interface. During spring tides, we observe vertical velocities vertically homogeneous with rapid inversions at each flood. The physical mechanism behind those observations will be pointed out in the next sections.

In summary, we highlight the tight relationship between the tidal forcing and the dynamical regimes developed around the sill. Two mains regimes are highlighted, the neap tide regime dominated by the baroclinic flow and the opposite spring tide regime largely dominated by barotropic flow. In both cases instabilities are likely to develop but with different physics that we will develop later. This analysis reveals that a small change in the strength of the barotropic flow, such as the tidal diurnal oscillation, can dramatically alter the small-scale processes that develop around the sill. This is observed between the 13 and 14 October when the typical spring tide dynamics is followed by typical neap tide dynamics. A close look at this period provides a threshold of $|\bar{U}_{\max}| = 1$ m/s for the transition between both dynamical regimes under the stratification conditions of the PROTEVS GIB20 experiment.

4.3. Spring Tides Dynamics

4.3.1. Overview

Over CS, the typical spring tide cycle presents five consecutive dynamical states, schematized in Figure 5. This figure sketches the main features of the three layers encounter over CS, Mediterranean Water (MW with typical salinity above 38 psu), Mixed layer (ML with typical salinity between 36.5 and 38 psu) and the Atlantic Waters (AW with typical salinity below 36.5 psu). Different observations support the existence of local hydraulic control, with associated hydraulic jump on the eastern flank of the main crest during the ebb (Figure 5a) which is released in a westward propagating Internal Solitary Bore (ISB) at the end of the ebb (Figure 5b). During the flood, isopycnals rapidly plunge over CS signaling the transitions from subcritical to supercritical flow (Figure 5c). With the increasing flood, the supercritical area extends westward leading to the formation of a larger hydraulic jump on the lee side of CS (Figure 5d). At this stage of the tidal cycle, the flow becomes supercritical above other smaller topographic features, giving rise to a network of local hydraulic jumps suggesting significant spatial variability due to the 3D topography of CS. Over the main crest, the flow is mainly barotropic and strongly turbulent, with an intense bottom layer developed in the Mediterranean outflow. At the end of the flood, the release of the hydraulic jump is observed through a eastward propagating ISB sometimes followed by a secondary mode (Figure 5e). For brevity, we characterize the flow with the last tidal cycle of the 15 October (Figure 6) and a few sections (Figures 7 and 8), but the general pattern is similar for all spring tides. In the following, we detail the different stages of the dynamics based on our observations.

4.3.2. Ebb Dynamics

At the reversal from ebb to flood, a westward propagation of an ISB is observed, signature of the release of a hydraulic jump formed during the ebb at the eastern side of the sill (schematized on Figures 5a and 5b). This hypothesis is supported by an acoustic images of a hydraulic jump east of CS observed during spring tide ebb (schematized on Figure 5a).

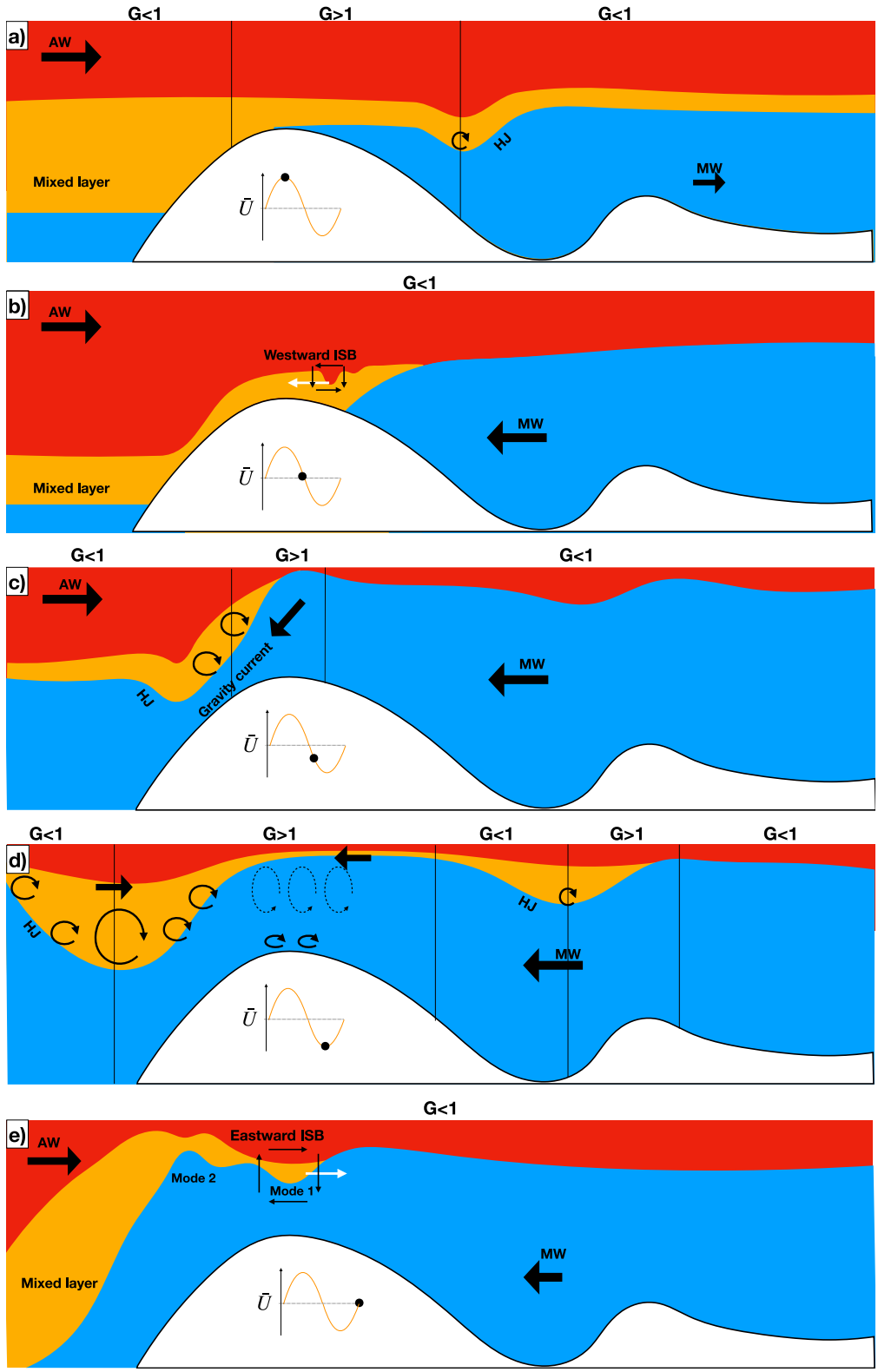

Figure 5.

The ADCP at MO2 captures a distinct signal in W and U at 18:45 (box f1 Figures 6b and 6c). The signature in W (negative, followed by positive vertical velocity between 18:30 and 19:00, followed by two smaller inversions until 19:15) characterizes the propagation of a large depression bore (followed by two smaller-amplitude variations). This signal is accompanied with a negative anomaly of the zonal baroclinic current in the upper layer (box f1 Figure 6b) suggesting a westward propagation of the internal bore. Indeed, the negative vorticity (regarding meridional axes) of this internal signature suggests westward propagation of a depression ISB (Figure 5 of Shroyer et al. (2009) or Figure 11 of Kurkina et al. (2018) for details). If this criterion is not sufficient to guarantee westward displacement in what should be highly 3D, the timing of this observation (end of the ebb) supports this hypothesis. In addition, during the spring tide ebbs the flow runs eastward in the whole water column (Figure 4b). Its maximal speed, reaches $U_{max} \approx 3$ m/s, such that the flow is locally controlled and we can expect the formation of a hydraulic jump on the eastern flank of CS. A rough bound of the composite Froude number in these conditions, computed from a density variation of 3 kg/m^3 (maximum found in the SoG) and a 200 m wide Atlantic layer, gives $G^2 = 5$ which is highly supercritical.

The MVP data combined with the VMADCP currents along S4_1ST section performed during spring tide ebb, highlight locally supercritical flows over the sill during the maximum ebb (Figures 7a and 7c). In addition, it depicts a slight plunge of the isopycnals on the eastern side of the sill (−5.715°W). The acoustic image confirms the plunge of the interface east of the sill and its rises just after (near −5.705° W on Figure 7a). Unfortunately, we did not perform density profile east of 5.71°W able to confirm local transition from supercritical to subcritical, but the acoustic image shows a hydraulic jump (rapid rise of the acoustic interface signing for the halocline) at −5.705°W which suggests a transition from locally supercritical to locally subcritical flow.

The temperature signal at the bottom at MO2 provides additional hints on the dynamics at the end of the ebb. The sensor shows that 2 hours before low tide (at 17:00), the temperature rapidly increases from 13.3° to about 14.2°C which are typical values for mixed waters (Figure 6f). This illustrates the eastward advection of the Mediterranean waters, completely pushed out of CS during strong ebbs. Note that this bump in temperature is in phase with the slowdown of the Mediterranean outflow marked by the absence of negative vertical velocity (Figure 6c). Jointly with the internal signature observed in W (previously discussed), the HF temperature signal oscillates rapidly at about 19:00 (Figure 6f). This shows that the westward propagating ISB propagates deep enough for the disturbance to reach the bottom.

The hydrological moorings at MO1 and MO3 capture this dynamics as well. At MO3, the 36.5 psu halocline exhibits a clear depression wave at 19:10, which is preceded and followed by high frequency fluctuations of the 38 psu halocline (Figure 6h). Without current data at these moorings, we are not able to provide the propagation direction of the detected structure. However, the hydraulic jump depicted in the acoustic images along the S4_1ST in the southern channel of the Sill, must be released in a westward propagating bore as the one observed at MO2. This is consistent with the observations of internal solitary waves at MO1 at about 20:00 (Figure 6g).

In summary, the flow is locally supercritical during part of the ebb (compare S1_ST and S4_1ST Figure 7c), especially in the southern part of CS (S4) and over the main crest (MO2). This situation leads to a local hydraulic jump east of CS that we clearly observe through acoustic images. We identify the propagation of an internal signature at the end of the ebb over the sill (at MO2) and suspect the same behavior in the southern channel (at MO3). This signature is most likely to be the westward propagation of an ISB when the eastward hydraulic jump is released.

Figure 5. Sketches of the flow along S2 section during an intense spring tide cycle. (a) Ebb dynamics with locally supercritical flow over the sill and formation of a hydraulic jump eastward. (b) Westward propagation of Internal Solitary Bore (ISB) while the flow returns subcritical over Camarinal Sill (CS) at the end of the ebb. (c) Local control over CS at the beginning of the flood with an intense plunge of the isopycnals over the sill and small hydraulic jump when the flow returns to subcritical over the western slope. (d) Extension of the locally controlled area over CS in the increasing flood with the displacement and growth of the hydraulic jump westward. Development of a turbulent bottom layer over the main crest. Development of similar hydraulic dynamics in smaller topographic features. (e) Release of the hydraulic jump over CS at the end of the flood with eastward propagation of mode 1 ISB followed by mode 2 in its tail. Note that black arrows represent current direction, white arrows the direction of wave propagation, black circular arrows shear instabilities and dashed circular circle turbulence. AW corresponds to Atlantic waters and MW to Mediterranean waters.

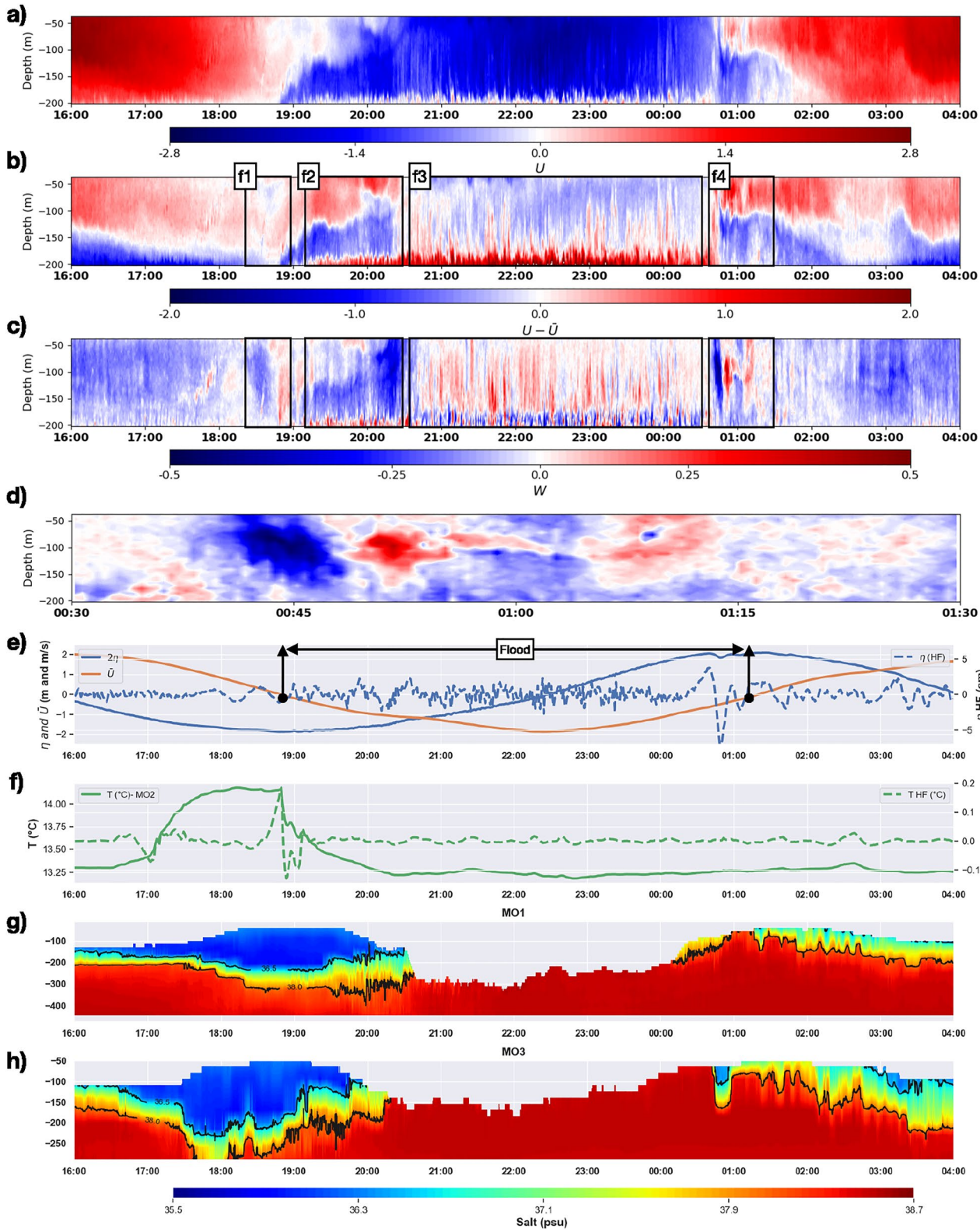

Figure 6. MO1/MO2/MO3 moorings data from 16:00 the 15 October 2020 to 04:00 the 16 October 2020. (a) Zonal current at MO2. (b) Baroclinic zonal current at MO2. (c) Vertical velocity at MO2. (d) Zoom of (c) on the black frame f4 (between 00:30 and 01:30 the 16 October 2020). Frames f1 to f4 are discussed in the text. (e) Sea level oscillation from pressure gauge (blue curve) and barotropic current (orange curve) at MO2. Dashed blue curve represents the high pass filtered pressure signal (at 1 hr period). (f) Potential Temperature at the bottom of MO2 (green curve) with its high-frequency signal (green dashed curve). (g, h) Salinity profiles at MO1 and MO3, respectively. The thin black lines correspond to the 36.5 and 38 psu isohalines.

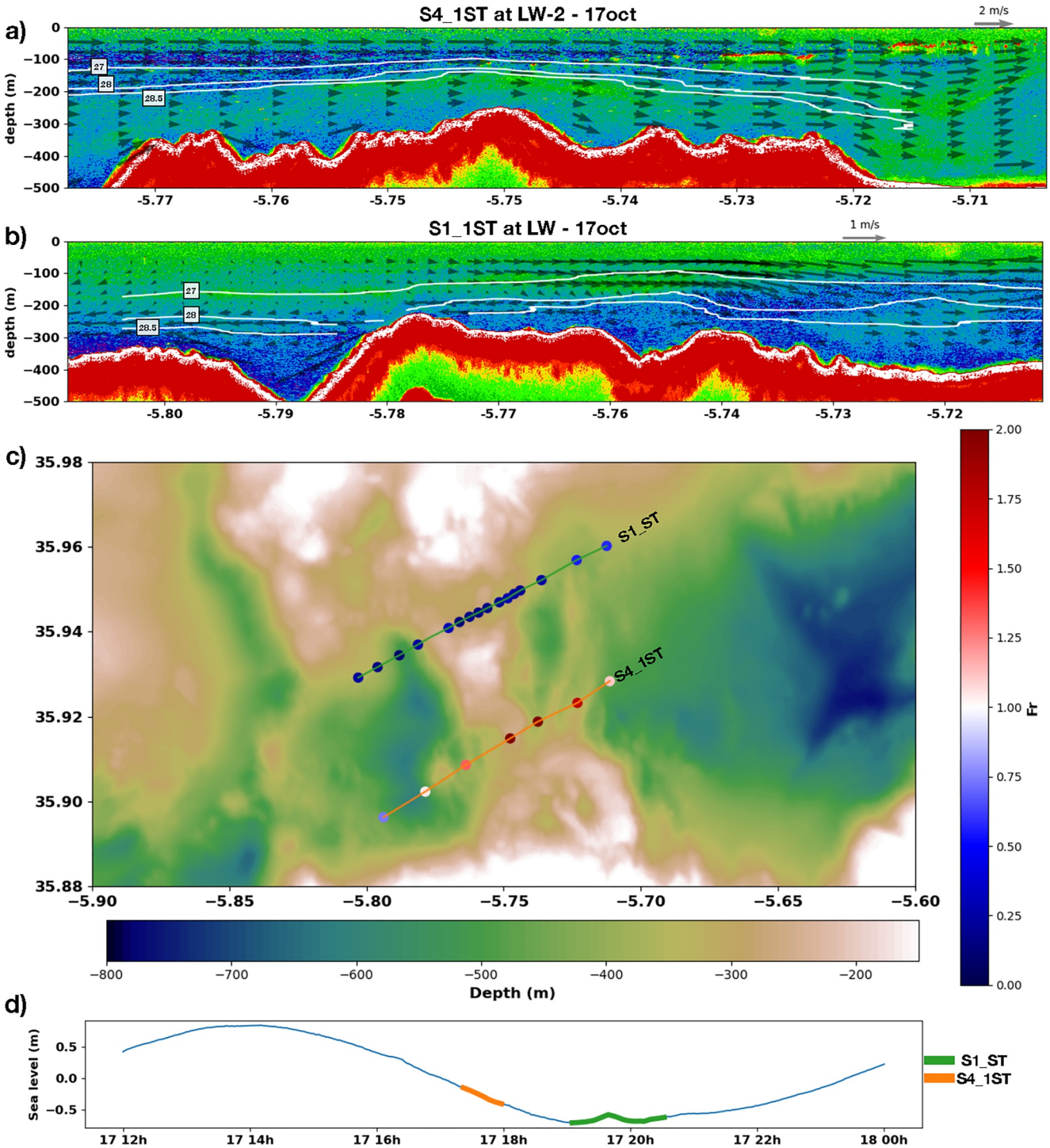

Figure 7. Sections (a) S4_1ST and (b) S1_1ST performed in spring tide ebb. The background color is the EK80 acoustic image at 38 kHz. The colors correspond to the intensity of the acoustic echo (in dB), the intensity increasing from blue to red colors. The thin white lines are the isopycnals of potential density 27/28/28.5 kg/m^3 computed from the interpolated Moving Vessel Profiler profiles along the section. Black arrows represents the current in the zonal/vertical plane from VMADCP at 38 kHz. (c) Bathymetric map of Camarinal Sill overlaps with the composite Froude number (see text for details on the computation method). (d) Sea level oscillation at Tarifa with the time of the sections superimposed by thick colored lines. The same colors are used to plot the sections route in panel (c).

4.3.3. Local Hydraulic Control Over CS in Early Flood

With the increasing flood, the Mediterranean layer growths before a dramatic acceleration of the vertical velocity; it likely corresponds to the transition from a subcritical to a supercritical flow leading to an intense plunge of the isopycnals over the sill (Figure 5c). The Mediterranean layer thickens from 20 at 19:00 to 120 m at 20:20 (box f2 Figure 6b), advected from Tarifa Narrows. Then, it flows on the western flank of CS characterized by the negative vertical velocity of about 0.1 m/s (Figure 6d). At this state, the situation is favorable to the plunge of the Mediterranean water, denser, in the lighter mixed water on the west of the sill, under the effect of gravity (see the depth of the isopycnals west of CS at the end of the ebb in section S1_1ST in Figure 7b and the schematized pattern Figures 5b and 5c).

At 20:15, the vertical velocity accelerates from near 0 to negative 0.3–0.5 m/s within 15 min. Even if we do not have corresponding stratification information, such an acceleration of the negative vertical velocity indicates a plunge of isopycnals surface which accompanies the flow when changing from subcritical to supercritical (Lawrence, 1993).

Density profiles along the S3_ST section, performed a little further south (Figure 8a) show that about 2 hours after the start of the flood, the isopycnals plunge over the sill. The computation of the Froude number along this section, confirms the criticality of the flow over the sill at this stage of the flood with a transition at the beginning of the western slope (Figure 8d). Note that the drop of isopycnals follows the local transition from supercritical to subcritical flow as theoretically expected (Armi & Farmer, 1986; Lawrence, 1993), but the isopycnals do not evidence a clear hydraulic jump eastward while the acoustic image highlights a small rebound at −5.765°W. At this stage the control should remain localized over the main feature of CS triggering a small hydraulic jump that the MVP horizontal resolution is not able to detect.

In summary, during the first hours of the flood the flow becomes supercritical over CS, accompanied with a drop of the isopycnals over the CS which accelerates the negative vertical velocity. The control is likely to remain localized over the main crest of the sill. Westward the section shows subcritical flow, but at the transition from supercritical to subcritical flow the isopycnals do not clearly rebound. However, the acoustic images highlights a rebound of the interface at the beginning of the slope that suggests a local hydraulic jump (Figure 8a).

4.3.4. Westward Extension of the Local Hydraulic Control

At the peak of the flood, the hydraulic transition (supercritical to subcritical) is shifted by the tidal current to the west of the sill and 3D turbulent high frequency processes are observed over the sill (Figure 5d). The Atlantic jet is blocked (at least deeper than 40 m) making the flow fully barotropic and strong mixing takes place.

At 20:45 an abrupt change is observed in the ADCP data at MO2, with a high frequency variability of the vertical velocity (Figure 6d). The transition is also noticeable in the horizontal baroclinic velocity profiles (Figure 6b), which presents a high frequency variability. The S2_ST section, performed during the maximum flood (4 hr after the start of the flood) confirms the westward advection of the hydraulic jump with the extension of the locally controlled area (Figures 8b and 8d). The isopycnals plunge on the western side of the sill (at 5.775°W), the flow over the sill is highly supercritical with composite Froude numbers higher than 3 (S2_ST on Figure 8d). This illustrates the transition from crest-controlled to what locally resembles a theoretical supercritical (Lawrence, 1993) or uncontrolled (Armi & Farmer, 2002) two-layer flow with no lateral variations. The hydraulic jump (rebound of the isopycnals) is colocalized with the transitions from supercritical to subcritical on the lee side of the Sill (5.78°W). Associated with this large bore west of CS, we can observe a mixing pattern both in the acoustic signal where the strong interface rolls-up (red-orange shade on Figure 8b), and the 28.5 kg/m^3 isopycnal detaches in a 100 m wide circular pattern resembling the huge shear instabilities discussed by Wesson and Gregg (1994).

East of the main crest (around 5.73°W), a slightly similar pattern occurs, with a smaller internal signature resembling a hydraulic jump, formed west of the bathymetric feature near −5.74°W. The EK60 at 38 kHz acoustic image confirms the hydraulic jump structures on the western flank of each crest (Figure 8b). The smaller structure signals the local transition from subcritical to supercritical over the bathymetric feature to subcritical where the depth increases before CS main crest (Figure 8d). The S4_2ST illustrates another formation of two successive hydraulic bore along the southern channel (5.765° and 5.78°W Figures 8c and 8d). This argues for the presence of multiple topographic induced hydraulic jumps rather than a single one and involves a complex geometry of the hydraulic controlled area in both zonal and meridional directions.

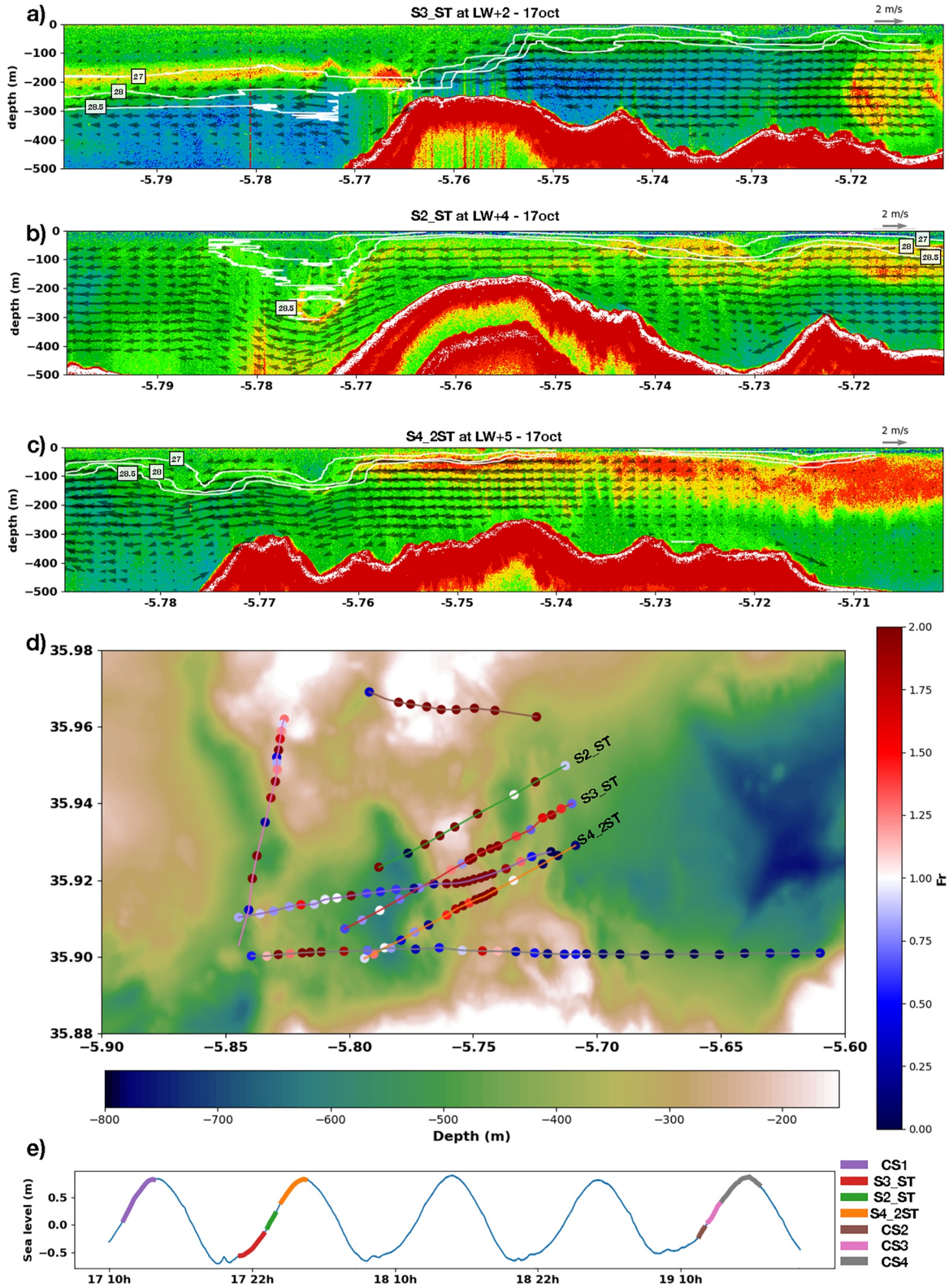

Figure 8. Same as Figure 7 for sections (a) S3_ST, (b) S2_ST, and (c) S4_2ST performed during one spring tide flood. (d) Bathymetric map of Camarinal Sill overlaps with the composite Froude number of the sections performed during spring tide floods. The three sections presented in panels (a–c) are labeled (see text for details on the computation method). (e) Sea level oscillation at Tarifa with the time of the sections superimposed by thick colored lines. The same colors are used to plot the sections route in panel (d).

Supercritical flow is associated with strong turbulence over the sill (at MO2) highlighted by high frequency oscillations of the vertical velocity (see Figure 6 between 20:30 and 00:45). The dynamics of the turbulent bottom boundary layer seems quite different from the rest of the water column. In the bottom layer (the 30 deepest meters) an energy spectrum of the vertical velocity W signal (not shown) shows different well resolved peaks at 4–6 min period with a more spread out peak between 12 and 14 min. Such an energy concentration suggests the presence of bottom vortices of different sizes in the boundary layer, characteristic of shear-overturns. Bottom layer development starts when the Mediterranean waters are advected to the west: it develops progressively with a height of 10 after 19:00 up to 30 m at the maximum ebb. Thus the bottom drag due to the rough topography could to be the dominant phenomenon for the development of such vortices. Different topographic roughness along the path of the current should explain the typical sizes. Above the boundary layer, the energy is more spread over a 13 min spike. Different hypotheses might explain the observed high frequency processes in the water columns. The first hypothesis is local instabilities created in the wake of isopycnals drop. The second hypothesis is a remote creation of these turbulent structures advected in the westward tidal current. S2_ST and S3_ST sections show that the topography presents another small sill east of CS which supports a smaller hydraulic jump (schematized Figure 5d). The turbulent processes, which develop there, could be advected over CS by the flood.

Another interesting feature is the presence of internal wave with a south-north signature, which are able to propagate with a cross-strait component in a meridionally sub-critical flow. In fact at 21:20, in the upper 150 m, we clearly distinguish an ISW signature in the vertical speed and in the baroclinic zonal current (Figures 6c and 6d). This pattern is associated with a noticeable signature in the meridional speed (not shown), that suggests meridional propagation of internal waves. The presence of such a structure shows the strong 3D feature of the dynamics around the sill, which is far from an idealized uniform south-north sill. Sánchez-Garrido et al. (2011) observed in their simulations meridional fronts at both southern/northern ends of CS. This observation confirms the model outcomes that north/south heterogeneity of the flow is significant over CS in addition with the 3D pattern of the controlled hydraulic zone. Note that such an internal wave is not observed at each flood.

This turbulent dynamics observed at the top of CS (MO2) extends spatially in the southern channel of the sill. Indeed, at MO3 the 38 psu halocline shows high frequency fluctuations combine with a rapid increase in the width of the halocline between 18:00 and 20:00 supporting the idea of a local transition from subcritical to supercritical (Figure 6h). However, in the growing current our mooring rapidly loses the interface layer at the peak of the flood, but the noticeable bore observed at 00:50 supports the existence of hydraulic control in the southern vein. The spatial extension of hydraulic control during spring tide floods is evidenced by the different sections performed over the Sill at this stage (Figure 7d). Even if these sections vary over the flood (Figure 7e), they highlight local hydraulic control from the south to the north of CS, which suggests that all the cross-strait section above CS is controlled at some time of the flood. The last remark concerns the meridional section CS3, that illustrates local control over a smaller topographic feature in the Tangier Basin that have been observed in the model of Sánchez-Garrido et al. (2011).

In summary, the strong flood extends the locally controlled region to the west, and pushed the isopycnals plunge on the lee side of the sill (Figures 5c and 5d). We observe hydraulic transitions, with hydraulic bores at almost all prominent bathymetric features arguing for a network of local hydraulic jumps (Figure 5c). All the cross-strait section above CS are controlled at the peak of the flood but with cross-strait variability in the zonal extension of the controlled area.

4.3.5. Release of the Hydraulic Jump

Finally when the flood decreases, the hydraulic jump is released into an eastward propagating ISB. It is detected at MO2 at 00:45 with a rapid changes in the vertical velocities from −0.3 to 0.3 m/s in 15 min (Figure 6c). This clear mode 1 internal bore is followed by a complex internal structure at 01:00 (Figure 6d). It might be a higher mode internal bore characterized by the inversion of the vertical velocity at about 100m below the surface (resembling a mode 2). The bores are also detected in high frequency pressure signal at MO2 (high depression in the HF η signal Figure 6e). Note that in contrast to the westward propagating bore discussed in Section 4.3.2, there is no signal of the eastward propagating bore in bottom temperature at MO2 (Figure 6f). This asymmetry is due to the shallower depth of the interface supporting the propagation of the internal bore in this situation.

At MO3, we observe one bore perfectly in phase with the internal signature at MO2 (Figure 6h). The 38 psu halocline depression at 00:45 presents an amplitude of about 100 m. In contrast to what we observe at MO2, there

is no higher mode observed at MO3. Later, from 01:30 to 02:30, the 38 psu halocline shows internal oscillations. The S4_2ST section, achieved near MO1 and MO3, highlights a second hydraulic jump west of CS on a small topographic feature at 5.775°W (Figure 8c). Consequently, these oscillations could be interpreted as the signature of the release of this second hydraulic jump.

4.3.6. General Summary

Section 4.3, describes the complex dynamics of the flow during spring tides near CS with five repetitive phases schematized in Figure 5. At the reversal from ebb to flood, a westward propagating ISB is observed (Figure 5b) suggesting hydraulic jump over CS during the maximum ebb (Figure 5a). With the increasing flood, the Mediterranean layer thickens and accelerates acting as a tidally modified gravity current. When the flow becomes supercritical over the sill ($\bar{U} \approx 1$ m/s), the isopycnic surfaces collapse driving strong negative vertical velocities (Figure 5c). At the peak of the flood, the super/sub critical transition is advected westward forming a hydraulic jump on the lee side. Smaller topographic features around CS create a network of local hydraulic jumps (Figure 5d). Finally, when the flood decreases ($\bar{U} \approx 0.5$ m/s), the flow returns to subcritical over the sill, the hydraulic jump is released in a large-amplitude eastward propagating ISB possibly followed by a secondary mode in its tail (Figure 5e).

Few other points stand out from our observations. The complex 3D bathymetry involves a significant cross/along strait variability of the internal hydraulics. A meridionally uniform sill cannot explain all small scale dynamics; indeed many processes develop with a non-negligible cross-strait variation. Above the sill, turbulent processes develop both in the bottom layer and in the water column; this has not been described before, to our knowledge (Figure 5d).

4.4. Neap Tides Dynamics

4.4.1. Overview

The neap tide dynamics over CS have been less extensively studied in the literature. The main features were reported in the pioneering works of Armi and Farmer (1988) and Wesson and Gregg (1994) from the *Gibraltar Experiment*, which reported quite strong mixing with hydraulic control over CS and a hydraulic jump in the westward flank. Surprisingly, they did not report a bore generating by the release of this internal hydraulic dynamics. MO2 mooring, sections over the sill and a fixed station provide additional information to understand this complex dynamics and its consequences on the exchanged flow. The main findings are schematized in Figure 9 which relies on the scheme provided by Wesson and Gregg (1994). During the ebb, our observations confirm that the two layers are maintained over the sill with a thinning of the Mediterranean layer while the ebb tidal current increases. When it reaches it maximum once a day, the ebb current locally block the Mediterranean waters for 1 hour which is a generate case of hydraulic control over CS. Shear instabilities develop in the mixed layer (Figure 9a). During the flood, we report similar observations as the former authors, with a plunge of the dense Mediterranean waters on the lee slope over the effects of tides and gravity. In addition to the shear instabilities in the interfacial mixed layer previously reported, we highlighted large overturns along the slope suggesting reversal of the Mediterranean outflow acting as a strong gravity current (blue inverse tongue Figure 9b). We exhibit a 20 m thick turbulent boundary layer over the main crest enhanced by the tidally accelerated Mediterranean outflow (bottom turbulence over the main crest Figure 9b).

4.4.2. Dynamics at the Sill

The neap tide dynamics at CS is different in many aspects from the spring tides dynamics. It does not present any abrupt regime transition, as the flow remains subcritical, except when the Mediterranean waters are locally blocked over the main crest of CS. However, many small-scale turbulent processes can develop, especially at the interface between the Atlantic and Mediterranean layers that are maintained almost throughout the tidal cycle. Daily rather than semi-diurnal pattern is exhibited due to the noticeable impact of the diurnal current (Candela et al., 1990; García-Lafuente et al., 1990); thus we illustrate this dynamics with two tidal periods (ADCP measurements the 11 October Figure 10). This period overlaps with the CTD casts performed during the FP station. Note that the first ebb is more intense than the second due to the diurnal oscillation of the tidal current.

In neap tide, the thickness of Mediterranean layer does not exceed half the depth over the sill, with a constant Atlantic jet flowing in the upper part of the water column (Figure 10b). The height of the Mediterranean layer

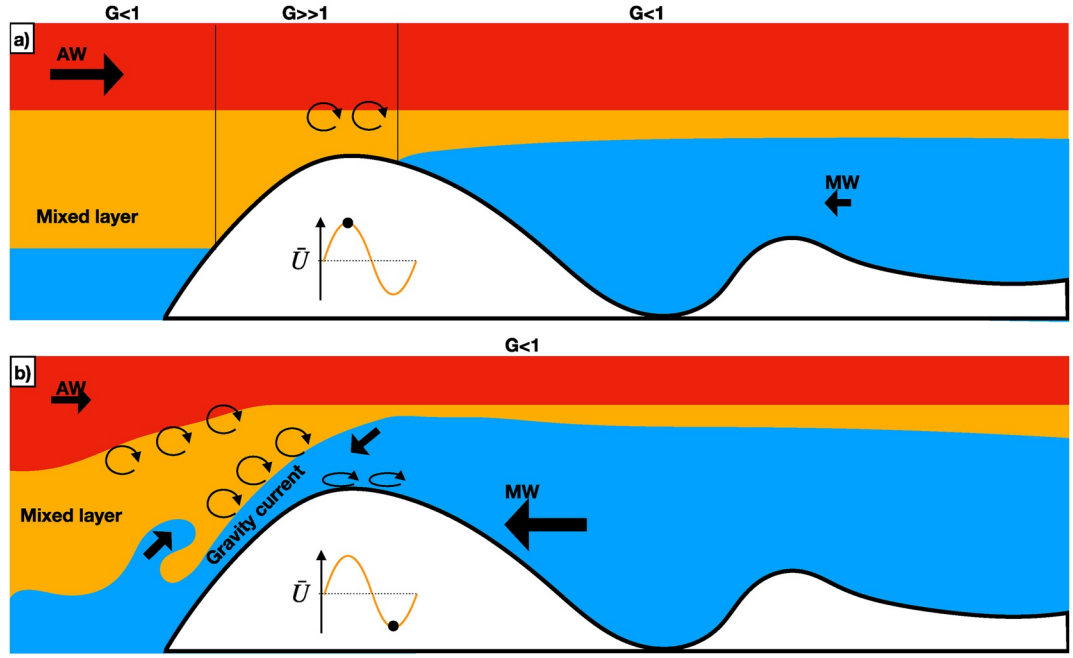

Figure 9. Sketches of the flow dynamics along S2 section in neap tide. (a) Ebb dynamics with advection of the Mediterranean water to the east and development of shear instabilities at the interface. (b) Flood dynamics the Mediterranean layer thickens and plunges in the mixed layer on the western flank of the sill generating instabilities at the interfaces. Reversal of the Mediterranean current inducing large overturns, and development of a bottom layer above the main crest. Note that black arrows represent current direction, black circular arrows shear instabilities. AW stands for Atlantic waters and MW for Mediterranean waters.

increases with the flood, illustrating the neap tide ability to advect Mediterranean waters from the Tarifa Narrows basin. The latter stops once a day, when the ebb reaches is diurnal maximum, which perfectly illustrates the impact of the tidal diurnal oscillation in the dynamics of the SoG. The local blocking of the Mediterranean water is illustrated along section S2_1NT shown in Appendix B.

The main difference with the spring tide period stands in the fact that the flow appears to remain subcritical throughout the flood phase (Figure 11d). During this phase, no regime transition occurs compared to the spring tide case. The vertical velocity decreases smoothly without abrupt acceleration (Figure 10d). It remains negative due to the continuous flow of the dense Mediterranean waters in the mixed water on the lee side of CS (acting like a gravity current). The sections, performed in neap tide floods, perfectly illustrate that the flow remains locally subcritical everywhere above CS (at least where we sampled) as illustrated in Figure 11d. However, along the three depicted sections we observe a plunge of the interface between Atlantic and Mediterranean waters (around −5.75°W for S4_NT, −5.753 for S2_2NT, and −5.755°W for S3_NT) which is the interface adjustment to the flow acceleration over the Sill characteristic of hydraulic control (Chen et al., 2017; Farmer & Smith, 1980; Lawrence, 1993; Sánchez-Garrido et al., 2011). Along S2_NT the deepest isopycnal depicted, as well as the acoustic interface, shows a clear rebound (−5.775°W in Figure 11b). The mechanism behind this observation remains quite unclear, but it resembles the internal trapped waves described by Bruno et al. (2002) for the same range of (locally subcritical) Froude numbers. The physical origin of these internal signatures is more deeply discussed in Section 5.4.

The sheared interface between the Atlantic layer and the Mediterranean layer is the place of instabilities development. After the maximum flood (between 20:00 and 23:00 Figure 10c), the Mediterranean outflow reaches is maximum (maximum baroclinic u). Then, alternative positive and negative vertical velocities at the interface characterize anticlockwise billows in the xz-plane related to shear instabilities (Figures 10d and 10e). This is supported by a positive anomaly of the baroclinic zonal flow in the AW layer and negative anomalies in the MW layer near the interface (Figure 10c). An energy spectrum of the vertical velocity signal averaged in the interface layer (75–175 m) performed during the flood (17:00 to 22:30 the 11 October) reveals that the energy is spread over different time-scales. The dominant peak is at 20 min, with an averaged current of 0.1 m/s in this layer during

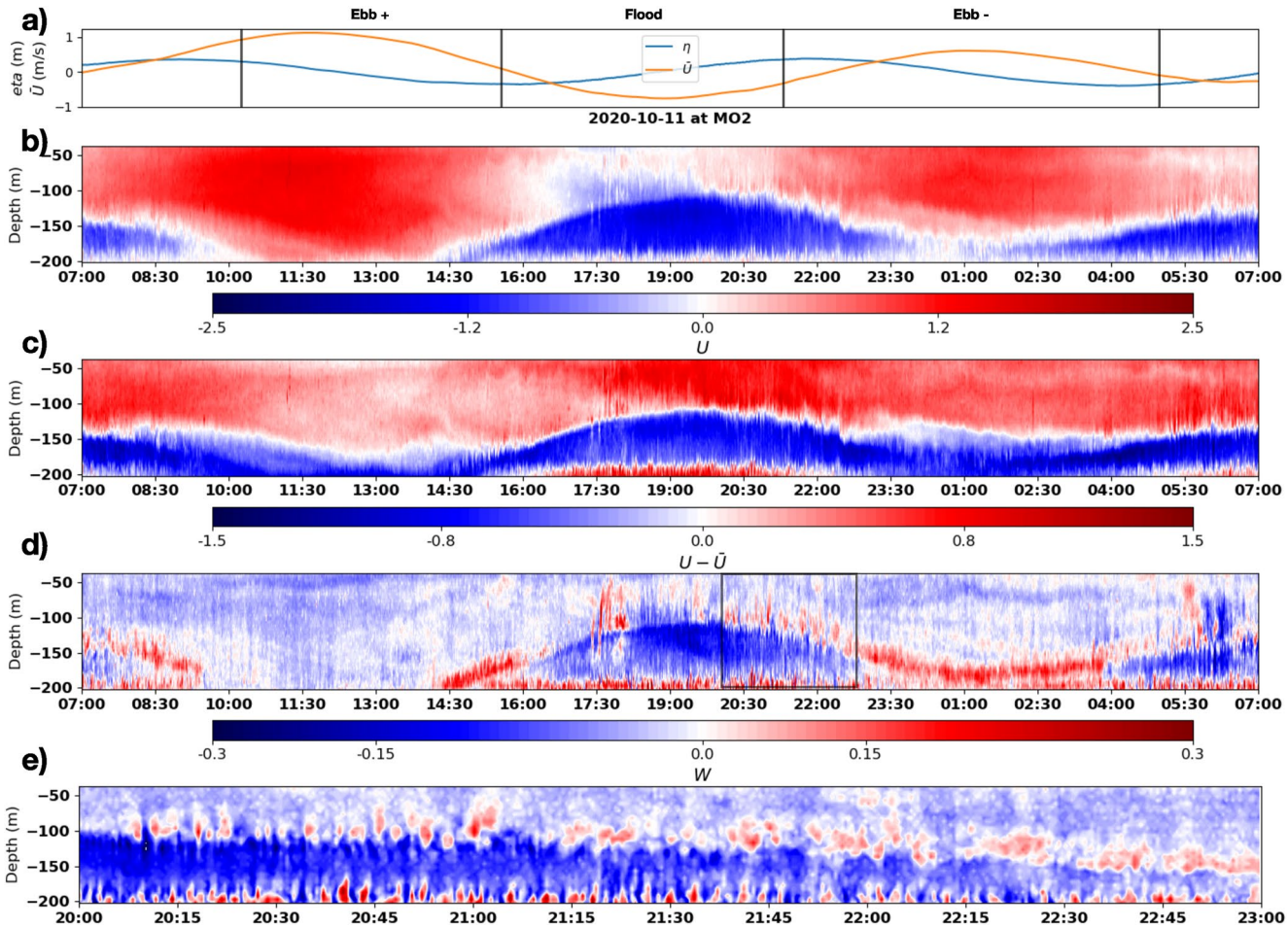

Figure 10. MO2 mooring data from 07:00 the 11 October 2020 to 07:00 the 12 October 2020. (a) Sea level oscillations (blue curve) and barotropic zonal current (orange curve) (b) zonal current. (c) Baroclinic zonal current. (d) Vertical velocity. (e) Zoom on the black box of panel (d).

this lapse of time we can roughly estimate the primary turbulent structure to be 120 m in length and on 50 m high. In addition, the HF-filtered isohalines in MO1 and MO3 show notable fluctuations during the same time period, with a typical period of 10 min for MO3 at 100 m depth (not shown).

4.4.3. Mediterranean Outflow

The FP station performed west of CS the 11 October between 14:00 and 19:00 depicts some characteristics of the turbulent structures formed when the Mediterranean waters flow downslope. We observe strong inversions of the zonal current in the Mediterranean layer at the peak of the flood, which extend up to 150 thick at 300 m depth (schematized by blue tongue reversal on Figure 9b).

The variability of the density profiles observed between the descending and ascending CTD casts evidences the rapid evolution of the Mediterranean outflow under increasing current (Figure 12a). While the Mediterranean outflow is not developed yet (at P1), the profile remains similar during one CTD cast with a clear seasonal thermocline at 30 m depth and the net halocline at the transition from Atlantic water to mixed waters at 180 m depth. Deeper than 300 m the density is slightly increasing in the Mediterranean waters (P1 in Figure 12a-left). In contrast, when the Mediterranean outflow starts flowing (at P2), we observe an important evolution of the density profile in a few minutes (about 15 min between descending and ascending casts), with the apparition of a sharper density gradient between Mediterranean and Atlantic waters (P2 in Figure 12a-middle). The sharper gradient confirms the idea of a growth of the Mediterranean outflow pushing out interfacial mixed water during this short period of 15 min. This is clearly depicted by the associated current (Figures 12e and 12f). Finally, at the peak of the flood, the interface height grows up to 120 m depth with a smoother gradient suggesting a mixed transition.

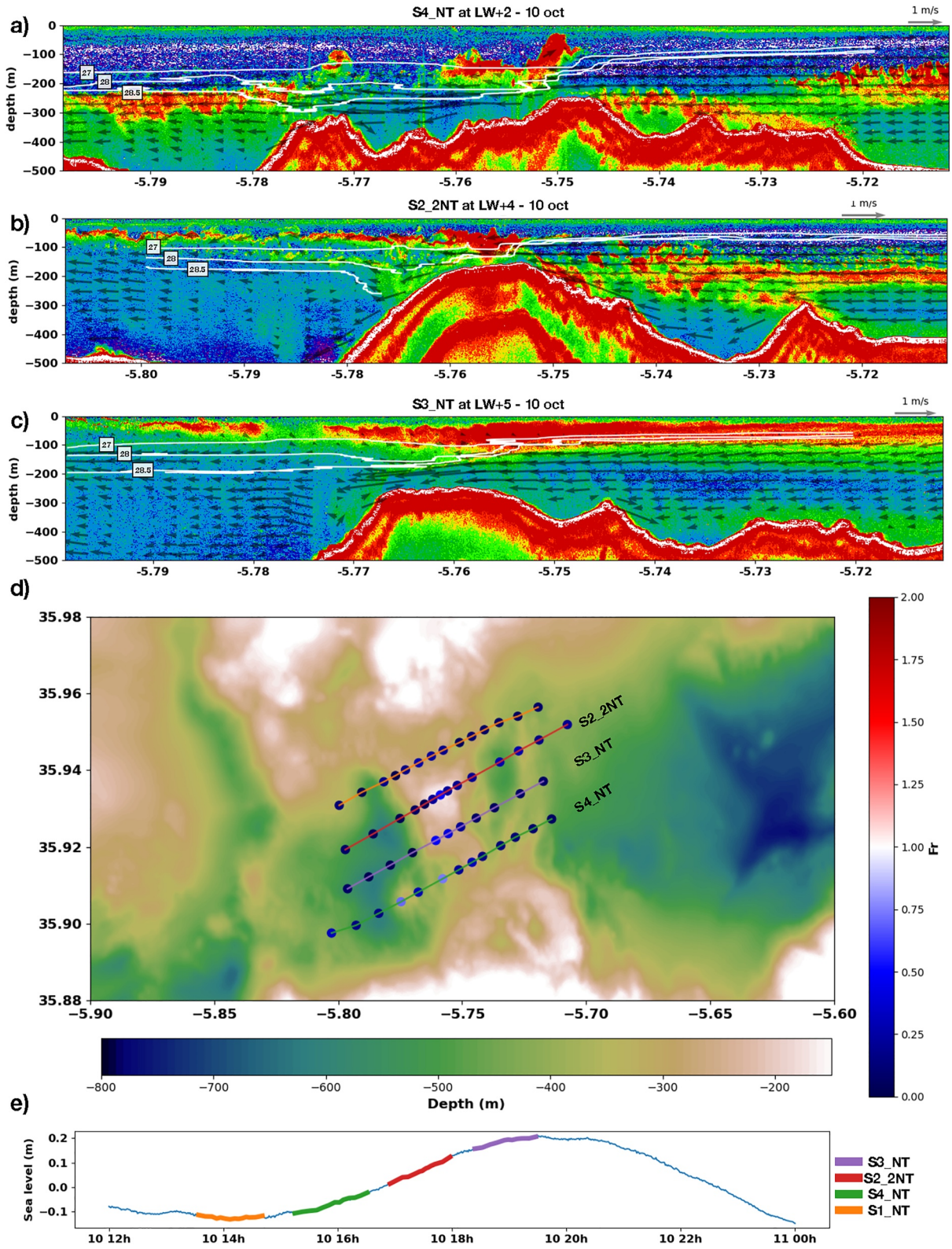

Figure 11. Same as Figure 7 for sections (a) S4_2NT, (b) S2_2NT, and (c) S3_NT performed during one neap tide flood. (d) Bathymetric map of Camarinal Sill overlaps with the composite Froude number of the sections performed during a neap tide flood. The three sections presented in panels (a–c) are labeled (see text for detailed computation method). (e) Sea level oscillation at Tarifa with the time of the sections superimposed by thick colored lines. The same colors are used to plot the sections route in panel (d).

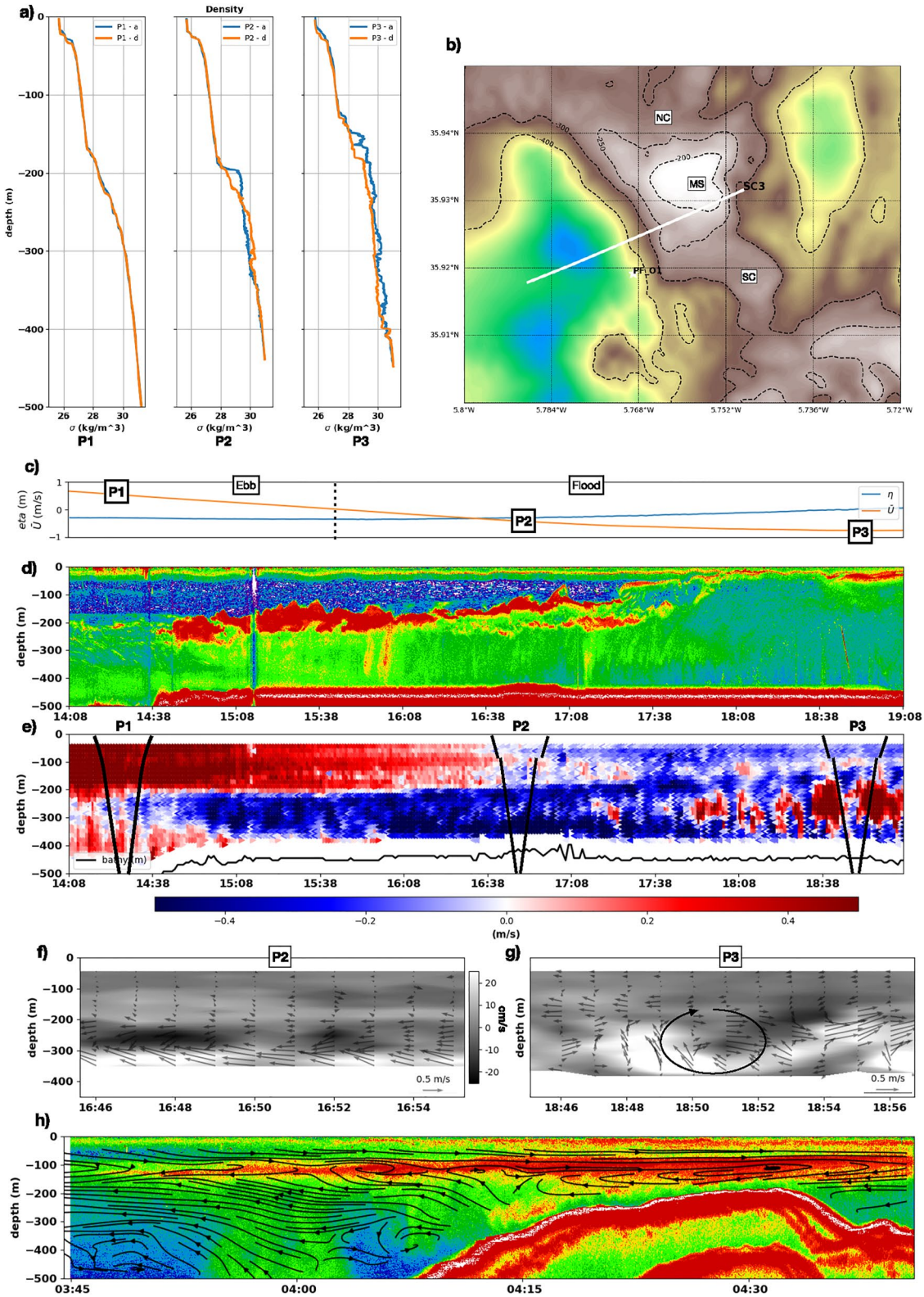

Figure 12.

Indeed, the acoustic image shows many instabilities slightly above the interface between Atlantic and Mediterranean waters (red interface around 200 m depth on Figure 12d) associated with zonal current variability near the interface (between 100 and 200 m depth after P2 profile on Figure 12e). These 50 m thick overturns are not the most impressive feature of the flow, where billows thicker than 150 m are observed during profile P3 (Figure 12e). The horizontal and vertical speed of the current gives some hints on the development of such structures (Figure 12g). At 18:48, eastward horizontal current is observed near 220 m depth associated with an intense upward signature (about 0.2 m/s). At 18:51, the flow is eastward on 150 m height with an intense downward signature (about −0.2 m/s). This is a clear feature of a large vortex developed in the Mediterranean outflow where no acoustic interface is visible. This might be triggered by the detachment of the Mediterranean outflow from the slope. As a consequence, part of the current reverses in large billow generating strong mixing as schematized in Figure 9b.

This hypothesis is supported by the SC3 acoustic section (See map Figure 12b) performed over the sill in neap tide outflow the 8 October. In Figure 12h, we can visualize the intense acoustic backscatter detaching from the slope (following the streamlines just before 5.77°W), which is probably the signature of the depicted phenomenon. The vertical velocity signal supports this hypothesis with a strong upward current colocalized with the acoustic detachment signature. Note that on the western part of this image, fluctuations in the acoustic intensity are remarkable. They might result from gravity waves triggered by the detachment of the gravity current. Since they are no hydrological measurements along this section, this mechanism remains a hypothesis.

5. Discussion

5.1. Influence of the Low Frequency Flow

The present data set confirms a strong influence of the tidal strength on the small-scale processes developed near CS. During spring tides, the flood is strong enough to totally reverse the Atlantic jet (at least deeper than 50 m) while in neap tide it remains persistent. This is coherent with the previous observations of Bryden et al. (1994) and the recent simulations of Gonzalez et al. (2023). The observations at MO2 illustrate that a small variation of the barotropic flow intensity can dramatically change the small-scale dynamics around the sill. For the stratification conditions of the GIB20 experiment, a threshold of about $\bar{U}_{\max} \approx 1$ m/s at MO2 is obtained for the transition between both regimes, similar to that given by Vásquez et al. (2008) using modeling. Lacombe and Richez (1982) suggest that the flow at CS can be decomposed in a long term, a subinertial and a tidal component. As discussed in the first section and as detailed in other studies (Candela et al., 1989; García-Lafuente et al., 2002; Vargas et al., 2006), the first two components present a slight variability at different time scales. This might influence the strength of the barotropic flow and thus that impacts the internal hydraulics and consequently the small scale dynamics as well as the exchange flow. For instance, Vásquez et al. (2008) show that the atmospheric situation over the Mediterranean basin can enhance internal wave generation at CS due to a slight increase of the westward subinertial flow.

5.2. Spatio-Temporal Variability of Hydraulic Control

The GIB20 experiment highlights the formation of a series of hydraulic jumps during spring tide floods. The largest hydraulic jump is formed over the main crest of CS (MO2) before being advected on the lee side with the increasing flow as previously observed (Armi & Farmer, 1988) and modeled (Hilt, 2022; Hilt et al., 2020; Sánchez-Garrido et al., 2011). Along with this well-known feature, we depict smaller hydraulic jumps formed over secondary topographic features west and east of the main crest that greatly complicate the hydraulic control around CS. The local composite Froude number reveals that jumps are concomitant with the transition from supercritical to subcritical flows as theoretically expected with the two layer approach (Armi & Farmer, 1986). This structure leads to strong isopycnal slopes up to the seasonal thermocline and velocity shears, source of

Figure 12. (a) Ascending (blue curves) and descending (orange curves) profiles of density anomaly from the three CTD casts performed during FP station. (b) Zoom over Camarinal Sill topography with the SC3 section plotted in white. NC corresponds to Northern Channel, SC to Southern channel, and MS to Main Sill. (c) Barotropic current at MO2 (orange curve) and sea level oscillation at Tarifa (blue curve) during FP station. (d) Acoustic image of the FP station from the EK80 echosounder at 38 kHz. The colors correspond to the intensity of the acoustic echo (in dB), the intensity increasing from blue to red colors. (e) Zonal current during FP station measured with the VMADCP 38 kHz instrument. Black thick lines superimposed represent the CTD ascending/descending casts. (f, g) Current in the zonal/vertical plane at the second and third CTD profile superimposed on the vertical velocity (gray shadow). (h) SC3 acoustic profile at 38 kHz performed the 8 October. Black lines superimposed represent streamlines.

many instabilities. It is consistent with microstructure measurements collected by Wesson and Gregg (1994), who observed structures of a few tens of meters west of the sill. In their simulations Hilt et al. (2020) show Kelvin-Helmholtz billows of tens of meters.

The complex structure of the local hydraulic control due to the dominant 3D feature of CS highlights the necessity of being cautious while modeling the SoG through 2D across-strait averaged models and shows the interest of fully 3D non-hydrostatic modeling as performed by Sánchez-Garrido et al. (2011). While it has long been known that the tide plays a key role in exchange flow in the SoG (Armi & Farmer, 1986), cross-strait variability was poorly assessed prior to the 3D modeling effort of the SoG. Our results highlight the strong zonal and meridional variability of the local nature of the flow, with hydraulic jump associated with smaller topographic features. The local nature of our results limits their interpretation in terms of global hydraulic control, but they clearly demonstrate the role of complex topography for small-scale processes and thus for mixing at CS.

The release of the hydraulic jump formed on the western flank of CS generates a solitary bore propagating eastward in the Mediterranean Sea while the flood slackens. Through ADCP measurements at MO2, we clearly identify a mode 1 ISB, generated first, followed by a smaller internal signature suspected to be a mode 2 (Figure 6e). At MO3 conversely, we only observe a mode 1 ISB. The ability of sills to generate a mode 2 internal solitary bores has already been observed in idealized simulations by Bordois et al. (2017), and more recently in realistic simulations by Hilt et al. (2020). Such a mode has previously been observed in different studies (Armi & Farmer, 1988; Vásquez et al., 2006). The generation of an ISB of higher modes strongly depends on the topographic length scale (see Figure 6 of Bordois et al. (2017)). As the sill width varies significantly meridionally, the generation of such mode could be very local. Once more, this observation highlights the role of the complex topography in the generation of the bore and can explains the complex shape of the internal solitary waves that propagates in the SoG (Vlasenko et al., 2009).

The GIB20 data set emphasizes that local blocking of the Mediterranean water occurs once a day in neap tide ebbs and hydraulic control occurs during strong ebbs, with the expected hydraulic jump on the eastern side of the sill. ADCP data highlight the westward propagation of an internal signal of mode 1 at the end of the ebb. A discussion with the authors of Hilt et al. (2020) confirms the presence of an internal signal propagating westward over the sill at the end of the ebb in their simulations. Sánchez-Garrido et al. (2011) observed such a structure in their 3D simulations as well. Even if such dynamics was suggested by Armi and Farmer (1988), and indirectly (through ADCP velocities fluctuations) observed in the northern channel of CS (García-Lafuente et al., 2018), this is a the first direct observation of a hydraulic jump during the ebb at CS. An important point, is that we suspect the same dynamics in the southern channel of CS as we observed internal fluctuations at MO3 at the end of the ebb. This result jointly with the observations of (García-Lafuente et al., 2018) in the northern channel suggest that hydraulic control happens at different locations of CS in at the maximum ebb of strong spring tides and thus should impact the exchange flow.

This finding questions the sparse observations of westward propagating ISW only reported by Alpers et al. (1996). The authors suggested that these waves were supported by the seasonal thermocline rather than with the Atlantic-Mediterranean halocline. We exhibit an asymmetry in the depth of the interface supporting eastward/westward ISB with the ability of bottom temperature probe to capture this signal. The westward propagating ISB develops deeper than the eastward propagating one. As a consequence the signature in surface is expected to be weaker, which can explain the scarcity of westward propagating ISB satellite observations and support the Alpers et al. (1996) hypothesis.

5.3. Mediterranean Outflow

During the neap tides floods, the dynamics is dominated by subcritical flow without large depressions of isopycnals but a Mediterranean outflow flowing on the lee side of CS. The Atlantic jet flows above the Mediterranean layer, whose thickness is controlled by the barotropic current. We identify instabilities at the interface between the two layers especially during the second part of the outflow. We investigate the nature of this instabilities through the excursion parameter $Ex = u_0/\omega l$, with ω, u_0 the tidal pulsation and amplitude, l the topographic lengthscale. The north-south varying topography of CS gives a typical lengthscale of 2,000 ± 500 m, for a neap tide amplitude of $u_0 = 0.2$ cm in the SoG (Figure 2a at MO4) at the M2 frequency, it gives $Ex = 0.7 \pm 0.2$, which is $O(1)$. Following the Laurent and Garrett (2002) criteria for lee waves developments we cannot expect lee waves during

neap tides over CS (observed at MO2) as the Excursion parameters falls below 1. However, Jalali et al. (2014) from direct numerical simulation at the laboratory scale (with constant stratification) showed possible development of transient lee waves for excursion parameter of 0.4. Even more, lee waves in sills with $Ex < 1$ parameter have been observed in other place (Buijsman et al., 2010; da Silva et al., 2015), which suggests to be cautious before excluding lee waves development over CS. Nevertheless, we test computed Richardson numbers along MVP profiles performed in neap tide floods, the results obtained are noisy but a distinctive patterns of low Richardson number ($Ri \leq 0.25$) at the interface appears (not shown). This analysis suggests that the vertical velocity sign-inversions observed at the interface during the neap tide floods are characteristic of shear instabilities but a deeper analysis, possibly through numerical simulations, are necessary to draw finals conclusions.

During neap tide, the FP station, performed on the west flanck of CS, highlights large overturns of about 150 m thick, twice as large as the ones observed by Wesson and Gregg (1994). Such overturns are much larger than expected from shear instabilities. Indeed, following Cushman-Roisin and Beckers (2011) the vertical extent of the mixed interface in shear instabilities in an infinite zonal flow of infinite depth can be computed from Equation 1, where ΔH represents the thickness of the instability, g the gravitational constant, ρ_0 the typical density of sea water, u_i (resp. ρ_i) the current (resp. the density) in layer i.

$$\Delta H \approx \frac{\rho_0 (u_1 - u_2)^2}{2(\rho_2 - \rho_1) g} \tag{1}$$

In neap tide flood on the western slope of CS $u_1 - u_2 = 1$ m/s, $\rho_2 - \rho_1 = 30 - 27 = 3$ kg/m^3, $g = 9.81$ m^2/s, and $\rho_0 = 1030$ kg/m^3 as typical value. ΔH is about 18 m in this case which is 10 times less than our observations. Thus shear instabilities are probably not at the origin of those structures, but cannot be totally excluded regarding the limitation of this theoretical approach and the internal signatures observed in neap tide. In his experimental review, Baines (2008) argues that on the western slope of CS, the gravity flow behave as a plume rather than a smooth gravity flow with much entrainment rapidly mixing the current with the environment. In this case, Baines (2008) experiment illustrates that the head of the current overturns at some point. This phenomenon is likely to be the one observed at FP station. Another possible processes is the development of transient lee-waves as discussed above. More investigations should be conducted to fully understand the physics of these large overturns developing in the Mediterranean outflow but they are likely the phenomenon generating the huge turbulent dissipation rate observed by Wesson and Gregg (1994) on the western flank of CS in neap tide floods.

5.4. Other Straits

Other straits in the world ocean exhibit similar dynamics partly determined by the hydraulic criticality of the flow, associated with small-scale processes. This paper suggests that the three-dimensional features of the bathymetry can impact the small-scale processes, a property shared by different straits. In the Luzon Strait, the complex double ridge system is suspected to explain the steepening of the internal tide, generating ISWs widely observed in this region (Mercier et al., 2013). In the Bab al Mandab Strait, Pratt et al. (2000) illustrated the importance of the cross-channel topography variations in the hydraulic criticality of the flow, using an extended version of the Taylor-Goldstein equation. Gregg and Pratt (2010) exhibited how the bathymetric complexity of the Sill of Hood Canal renders the interpretation of the data set, based on the hydraulic theory, quite complex. This is a small sample of many results illustrating how 3D bathymetric features may impact the dynamics in straits. This supports the key role of non-hydrostatic 3D modeling combined with a fine-scale in situ data set, for a better understanding of straits dynamics.

Near CS we exhibit two different regimes following the tidal strength, that can be compared to the regimes described in Knight Inlet (British Columbia). Farmer and Smith (1980) from a large in situ data set and more recently Chen et al. (2017) with 2D nonhydrostatic model highlighted three different regimes at Knight Inlet: in neap tide the flow remains subcritical over the sill but the steepening of the long wave due to the acceleration of the flow at the sill generates ISWs, in medium to strong tide the flow is supercritical upstream and a hydraulic jump is formed, which is released into a train of ISWs, and finally in very strong spring tide the upstream hydraulic jump is advected downstream in a turbulent hydraulic jump, released as a bore when the tidal current slackens. The last regime coincide with our observation over CS performed in very strong spring tide, showing a huge hydraulic jump on the lee side. Sánchez-Garrido et al. (2011) highlighted a pattern quite equivalent to the second regime of Knight Inlet with the formation and maintain

of upstream hydraulic jump over CS. Section S4 discussed in this paper (Figure 8c), depicts two relevant isopycnal depressions framing the topographic feature at −5.77°W (Figure 8c). The easternmost hydraulic jump resembles the upstream hydraulic jump observed in model and described at Knight Inlet. This observation suggests that different regimes can develop at CS due to the north-south variability of the topography and the tidal temporal variability. Finally, in neap tide we observed subcritical flow with a noticeable plunge of the isopycnals in the easternmost part of CS which resembles the subcritical upstream influence regime described at Knight Inlet by Chen et al. (2017). Another hypothesis is the existence of hydraulic control for higher mode, the Froude number for second mode is largely higher than one along this section (see Figure A1 in Appendix A), situation previously described at Knight Inlet by Farmer and Smith (1980). In addition, along S2_2NT we observed a depression of the isopycnals surface with instabilities on the western flank of CS associated to subcritical flow. The feature is quite similar to the transient lee waves depicted by Alford et al. (2015) in the subcritical flow of the Luzon Strait, which is thus another hypothesis complementary to the reversal of tidally modified gravity current that could explain the huge instabilities depicted on the western flank of CS in this study.

6. Conclusion

In this paper, we demonstrated that the main topographic feature of the SoG, CS, supports two distinct dynamical regimes that trigger the development of different small-scale processes. The strength of the barotropic current is highlighted to be the main driver of the variability as it impacts the hydraulic nature of the flow. In the stratification conditions of October 2020, the regime shift happens when the barotropic current $\left(\bar{U}\right)$ reaches 1 m/s. The variability of the barotropic current is dominated by the tidal fortnightly cycle, but other time scales can modulate its strength and therefore impact the small-scale structure development.

The extensive sections performed in spring tide floods show that the main crest of CS is hydraulically controlled but with a large variability of the local control both in time (tidal variability essentially) and space (3D topographic influence). This point questions the ability of 2D models to represent the complexity of the flow in the SoG and argues in favor of 3D modeling.

The spring tide ebb dynamics is not symmetric because of the sill asymmetry and of the baroclinic flow. However, intense barotropic ebbs make it locally controlled. We showed the development of an eastward hydraulic jump that is released in a westward propagating ISB at the end of the ebb. At this stage, the halocline is deeper, thus the bore surface signature should be weaker, explaining the difficulties to observe this westward propagation from space.

We finally focused on the neap tide dynamics. The baroclinic nature of the flow throughout the tidal cycle leads to shear instabilities at the interface between Mediterranean and Atlantic waters. During the flood, the Mediterranean outflow is enhanced by the tide flowing on the western flanck of CS in what appears to be a tidally modified gravity current. The gravity acceleration along the sharp slope is hypothesized to be the dominant processes generating large overturns (thicker than 150 m) in the Mediterranean outflow.

This complex dynamics strongly impacts the mixing of the water masses during their journey near CS. The next step is to quantify the turbulence dissipation rates triggered by the different processes and how they impact the mixing of the different waters masses encounter in CS region. This questions will be addressed in a dedicated paper.

Appendix A: Comparison Between Different Froude Number Computation

The Froude number computation rests on the choice of a model. We chose the two-layer model because it provides a composite Froude number and allows a tractable calculation of conditions for instability: locally supercritical flows are necessary for instabilities to develop as demonstrated in Appendix A1 of Sánchez-Garrido et al. (2011). In this two-layer model, we defined the interface as the halocline $S = 37.2$ psu, to follow Bray et al. (1995) findings over CS.

The present appendix illustrates the sensitivity of results to the definition of the interface and the sensitivity of the Froude number to the theoretical approach, which involves very different assumptions on the flow. Calculations

are performed along section *S*2_2NT in neap tide flood. As shown above, this section has locally subcritical flow all along; now, we investigate it with other models than the two-layer model.

We use the following models:

- Three layer model (Sannino et al., 2002): it consists of an extended version of the two layer composite Froude number which integrates a mixed layer. The Froude number in this case is computed in the following way:

$$G^2 = Fr_1^2 + Fr_2^2 + Fr_3^3 \tag{A1}$$

  where Fr_i the Froude number of layer i. If $r_{i,j}$ the ratio between the density of layer i and j, h_i its width, u_i its current averaged, and g the local gravity, we define:

$$Fr_1^2 = \frac{u_1^2}{gh_1(1-r_{1,2})},\ Fr_2^2 = \frac{u_2^2(1-r_{1,3})}{gh_2(1-r_{2,3})(1-r_{1,2})},\ Fr_3^2 = \frac{u_3^2}{gh_3(1-r_{2,3})} \tag{A2}$$

- The phase speed computed from the Taylor-Goldstein equation (Pratt et al., 2000). This is particularly suitable in presence of a strongly sheared background current $U(z)$. This model is derived from the 2D Euler equations in the Boussinessq approximation, neglecting the Coriolis force and the viscous dissipation. The phase speed c of the wave is the eigenvalue of the following eigenvalue-eigenvector problem:

$$(U-c)^2\frac{\mathrm{d}^2W}{\mathrm{d}z^2} + \left(N^2 - (U-c)\frac{\mathrm{d}^2U}{\mathrm{d}z^2}\right)W = 0 \tag{A3}$$

  where W the vertical velocity, N^2 the squared Brünt-Vaïsala frequency. The problem is solved numerically with the Dirichlet boundary conditions $W(0) = W(z_{bottom}) = 0$. Noting that the phase speed computed with Equation A3 embedded the advection by the tidal current, we computed the Froude number as the vertically averaged current which is hypothesized to represent the background current, divided by the phase speed retrieved from the from the background current. In this case $Fr = U/(c-U)$, in such a way that $Fr = 1$, when $c = U$ which corresponds to a controlled situation.
- The phase speed computed from long inertia-gravity wave. The phase speed in this case is computed from the following eigenvalue-eigenvector problem:

$$\frac{\mathrm{d}^2W}{\mathrm{d}z^2} + k^2\frac{N^2-\omega^2}{\omega^2-f^2}W = 0 \tag{A4}$$

  where g the local gravity, f the local Coriolis parameter, W the vertical velocity, k the wavelength, and ω the pulsation. The problem is solved numerically with the Dirichlet boundary conditions $W(0) = W(z_{bottom}) = 0$ in the long wave limit $k \to 0$. Then we computed the Froude number as the integral of the absolute zonal current divided by the phase speed of the first internal wave mode.

Figure A1 shows the Froude numbers computed with these different models along the S2_2NT section depicted in Figure 11b. We add a test of sensitivity to the isohaline choice for the two layer composite model. We provide the values for the Taylor-Goldstein equation with and without background current to assess the impact of the shear. The result highlights that shear has little impact on the phase speed near the Sill.

All the models provide consistent results, the flow is locally subcritical along the section. The two layer composite Froude number is not sensitive to a slight change in the choice of the isohaline. The shear current impacts noticeably the results even if it does not modify the nature of the flow.

Along S2_2NT, the second mode Froude number computed with the long inertia-gravity wave shows that hydraulic control happens for these waves over the Sill.

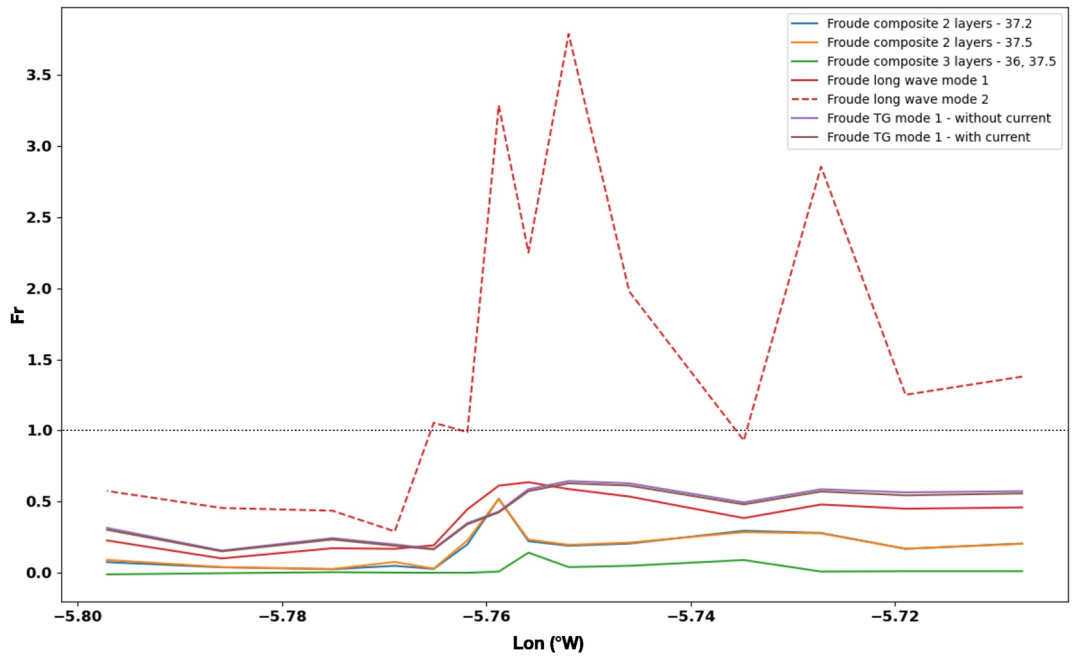

Figure A1. Froude number along S2_2NT section for different models (see text for details). 36, 37.2, and 37.5 (in psu) are the isohaline surfaces used to determine the interfaces for each model. Red dashed curve correspond to the same model than red curve but for second mode wave.

Appendix B: Section S2_1NT

Figure B1 presents the section S2_1NT performed two hours before the low water (ebb phase) the 10 October (neap tide). It illustrates the blocking of the Mediterranean outflow by hydraulic control during part of the neap tide cycle at CS.

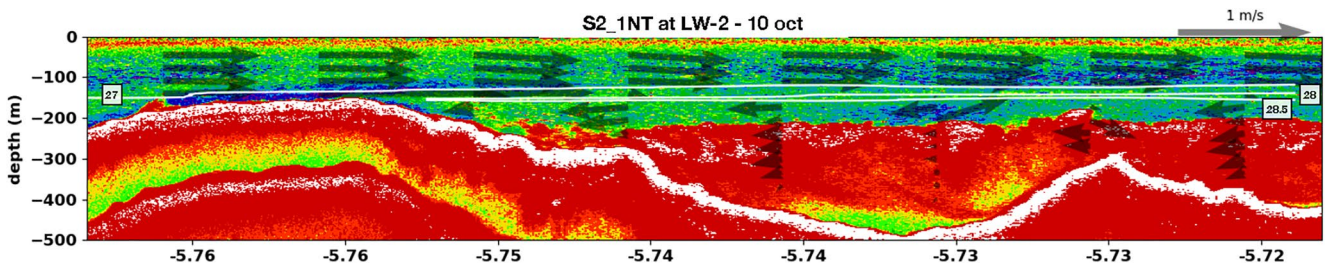

Figure B1. Sections S2_1NT performed in neap tide ebb. The background color is the EK80 acoustic image at 38 kHz. The colors correspond to the intensity of the acoustic echo (in dB), the intensity increasing from blue to red colors. The thin white lines are the isopycnals of potential density 27/28/28.5 kg/m^3 computed from the interpolated Moving Vessel Profiler profiles along the section. Black arrows represents the current in the zonal/vertical plane from VMADCP at 38 kHz.

Data Availability Statement

- The PROTEVS GIB 20 data used in this paper are available via this link https://www.seanoe.org/data/00819/93129/ (Bordois & Dumas, 2023).
- The Tarifa tide gauge data are available and downloadable on the web site of Puertos Del Estados, at this address http://opendap.puertos.es/thredds/catalog/tidegauge_tari/catalog.html (Puertos del Estado (Spain), 2023)
- The grid of the ARPEGE model reanalysis from METEO FRANCE (Courtier et al., 1991) are available in the METEO FRANCE webpage via the following link https://donneespubliques.meteofrance.fr/?fond=produit&id_produit=130&id_rubrique=51 (Meteo France, 2023).

Acknowledgments
We gratefully acknowledge the Direction Générale de l'Armement which funded the program Protevs II into which the GIB20 experiment at sea was scheduled, the French Naval Hydrographic and Oceanographic Service (SHOM), the "Flotte Oceanographique Française," FOF and the crew of the R/V "L'Atalante" (IFREMER) for their contribution to the GIB20 experiment preparation and implementation at sea. The SHOM teams in charge of the data collection and their quality control are thanked for their contributions. We are grateful to Puertos del Estado Institution (Spain) for freely providing the sea level data at Tarifa employed in this study.

References

Alford, M. H., Peacock, T., MacKinnon, J. A., Nash, J. D., Buijsman, M. C., Centurioni, L. R., et al. (2015). The formation and fate of internal waves in the south China Sea. *Nature*, *521*(7550), 65–69. https://doi.org/10.1038/nature14399

Alpers, W., Brandt, P., Rubino, A., & Backhaus, J. (1996). Recent contributions of remote sensing to the study of internal waves in the Straits of Gibraltar and Messina. *Dynamics of Mediterranean Straits and Channels*, *17*, 21–40.

Armi, L., & Farmer, D. (1985). The internal hydraulics of the Strait of Gibraltar and associated sills and narrows. *Oceanologica Acta*, *8*(1), 37–46.

Armi, L., & Farmer, D. (1986). Maximal two-layer exchange over a sill and through the combination of a sill and contraction with barotropic flow. *Journal of Fluid Mechanics*, *164*, 53–76. https://doi.org/10.1017/s002211208600246x

Armi, L., & Farmer, D. (1988). The flow of Atlantic water through the Strait of Gibraltar. The flow of Mediterranean water through the Strait of Gibraltar. *Progress in Oceanography*, *21*, 1–105.

Armi, L., & Farmer, D. (2002). Stratified flow over topography: Bifurcation fronts and transition to the uncontrolled state. *Proceedings of the Royal Society of London. Series A: Mathematical, Physical and Engineering Sciences*, *458*(2019), 513–538. https://doi.org/10.1098/rspa.2001.0887

Baines, P. G. (2008). Mixing in downslope flows in the ocean - Plumes versus gravity currents. *Atmosphere-Ocean*, *46*(4), 405–419. https://doi.org/10.3137/ao.460402

Bordois, L., Auclair, F., Paci, A., Dossmann, Y., & Nguyen, C. (2017). Nonlinear processes generated by supercritical tidal flow in shallow straits. *Physics of Fluids*, *29*(6), 066603. https://doi.org/10.1063/1.4986260

Bordois, L., & Dumas, F. (2023). protevs gib20 - Camarinal Sill [Dataset]. https://doi.org/10.17882/93129

Bray, N. A., Ochoa, J., & Kinder, T. (1995). The role of the interface in exchange through the Strait of Gibraltar. *Journal of Geophysical Research*, *100*(C6), 10755–10776. https://doi.org/10.1029/95jc00381

Bruno, M., Alonso, J. J., Cózar, A., Vidal, J., navate, A. R.-C., Echevarría, F., & Ruiz, J. (2002). The boiling-water phenomena at Camarinal Sill, the Strait of Gibraltar. *Deep-Sea Research II*, *49*(19), 4097–4113. https://doi.org/10.1016/s0967-0645(02)00144-3

Bryden, H. L., Candela, J., & Kinder, T. H. (1994). Exchange through the Strait of Gibraltar. *Progress in Oceanography*, *33*(3), 201–248. https://doi.org/10.1016/0079-6611(94)90028-0

Buijsman, M. C., Kanarska, Y., & McWilliams, J. C. (2010). On the generation and evolution of nonlinear internal waves in the South China Sea. *Journal of Geophysical Research*, *115*(C2), C02012. https://doi.org/10.1029/2009JC005275

Candela, J., Winant, C. D., & Bryden, H. L. (1989). Meteorologically forced subinertial flows through the Strait of Gibraltar. *Journal of Geophysical Research*, *94*(C9), 12667–12679. https://doi.org/10.1029/jc094ic09p12667

Candela, J., Winant, C. D., & Ruiz, A. (1990). Tides in the Strait of Gibraltar. *Journal of Geophysical Research*, *95*(C5), 7313–7335. https://doi.org/10.1029/jc095ic05p07313

Chen, Z., Nie, Y., Xie, J., Xu, J., He, Y., & Cai, S. (2017). Generation of internal solitary waves over a large sill: From knight inlet to Luzon Strait. *Journal of Geophysical Research: Oceans*, *122*(2), 1555–1573. https://doi.org/10.1002/2016JC012206

Courtier, P., Freydier, C., Geleyn, J.-F., Rabier, F., & Rochas, M. (1991). The arpege project at meteo France. *Seminar on Numerical Methods in Atmospheric Models*, *9–13*, 193–232.

Cushman-Roisin, B., & Beckers, J.-M. (2011). *Introduction to geophysical fluid dynamics physical and numerical aspects* (2nd ed., Vol. 101). International Geophysical Series.

da Silva, J., Buijsman, M., & Magalhaes, J. (2015). Internal waves on the upstream side of a large sill of the Mascarene ridge: A comprehensive view of their generation mechanisms and evolution. *Deep Sea Research Part I: Oceanographic Research Papers*, *99*, 87–104. https://doi.org/10.1016/j.dsr.2015.01.002

Farmer, D. M., & Denton, R. A. (1985). Hydraulic control of flow over the sill in Observatory Inlet. *Journal of Geophysical Research*, *90*(C5), 9051–9068. https://doi.org/10.1029/jc090ic05p09051

Farmer, D. M., & Smith, J. D. (1980). Tidal interaction of stratified flow with a sill in knight inlet. Deep sea research Part A. *Oceanographic Research Papers*, *27*(3), 239–254. https://doi.org/10.1016/0198-0149(80)90015-1

García-Lafuente, J., Almazán, J., Castillejo, F., Khribeche, A., & Hakimi, A. (1990). Sea level in the Strait of Gibraltar: Tides. *International Hydrographic Review*, *LXVII*(1). Retrieved from https://journals.lib.unb.ca/index.php/ihr/article/view/23321

García-Lafuente, J., Fanjul, E. A., Vargas, J., & Ratsimandresey, A. (2002). Subinertial variability in the flow through the Strait of Gibraltar. *Journal of Geophysical Research*, *107*(C10), 3168. https://doi.org/10.1029/2001jc001104

García-Lafuente, J., Pozas, E. B., Sánchez-Garrido, J. C., Sannino, G., & Sammartino, S. (2013). The interface mixing layer and the tidal dynamics at the eastern part of the Strait of Gibraltar. *Journal of Marine Systems*, *117–118*, 31–42. https://doi.org/10.1016/j.jmarsys.2013.02.014

García-Lafuente, J., Sammartino, S., Sánchez-Garrido, J. C., & Naranjo, C. (2018). *Asymmetric baroclinic response to tidal forcing along the main sill of the Strait of Gibraltar inferred from mooring observations. The ocean in motion* (pp. 193–210). Spinger.

García-Lafuente, J., Vargas, J. M., Plaza, F., Sarhan, T., Candela, J., & Bascheck, B. (2000). Tide at the eastern section of the Strait of Gibraltar. *Journal of Geophysical Research*, *105*(C6), 14197–14213. https://doi.org/10.1029/2000JC900007

Gascard, J., & Richez, C. (1985). Water masses and circulation in the western Alboran Sea and in the Strait of Gibraltar. *Progress in Oceanography*, *15*(3), 157–216. https://doi.org/10.1016/0079-6611(85)90031-x

Gomez-Enri, J., Vázquez, A., Bruno, M., Mariscal, L., & Villares, P. (2007). Characterization of internal waves in the Strait of Gibraltar, using SAR and in-situ measurements. *European Space Agency, (Special Publication) ESA SP*.

Gonzalez, N., Waldman, R., Sannino, G., Giordani, H., & Somot, S. (2023). Understanding tidal mixing at the Strait of Gibraltar: A high-resolution model approach. *Progress in Oceanography*, *212*, 102980. https://doi.org/10.1016/j.pocean.2023.102980

Gregg, M. C., & Pratt, L. J. (2010). Flow and hydraulics near the Sill of Hood Canal, a strongly sheared, continuously stratified fjord. *Journal of Physical Oceanography*, *40*(5), 1087–1105. https://doi.org/10.1175/2010JPO4312.1

Harzallah, A., Alioua, M., & Li, L. (2014). Mass exchange at the Strait of Gibraltar in response to tidal and lower frequency forcing as simulated by a Mediterranean Sea model. *Tellus A: Dynamic Meteorology and Oceanography*, *66*(1), 23871. https://doi.org/10.3402/tellusa.v66.23871

Hilt, M. (2022). Exploration des fines échelles océaniques dans le détroit de Gibraltar: Simulation numérique, observation et mélange induit.

Hilt, M., Auclair, F., Benshila, R., Bordois, L., Capet, X., Debreu, L., et al. (2020). Numerical modelling of hydraulic control, solitary waves and primary instabilities in the Strait of Gibraltar. *Ocean Modelling*, *151*, 101642. https://doi.org/10.1016/j.ocemod.2020.101642

Jalali, M., Rapaka, N. R., & Sarkar, S. (2014). Tidal flow over topography: Effect of excursion number on wave energetics and turbulence. *Journal of Fluid Mechanics*, *750*, 259–283. https://doi.org/10.1017/jfm.2014.258

Jia, Y. (2000). Formation of an Azores current due to Mediterranean overflow in a modeling study of the North Atlantic. *Journal of Physical Oceanography*, *30*(9), 2342–2358. https://doi.org/10.1175/1520-0485(2000)030<2342:foaacd>2.0.co;2

Kinder, T. H., & Bryden, H. L. (1987). The 1985-1986 Gibraltar experiment: Data collection and preliminary results. *EOS*, *68*(40), 786–794. https://doi.org/10.1029/eo068i040p00786

Kurkina, O., Rouvinskaya, E., Kurkin, A., Giniyatullin, A., & Pelinovsky, E. (2018). Vertical structure of the velocity field induced by mode-i and mode-ii solitary waves in a stratified fluid. *The European Physical Journal E*, *41*(3), 47. https://doi.org/10.1140/epje/i2018-11654-3

Lacombe, H., & Richez, C. (1982). The regime of the Strait of Gibraltar. *International Liege Colloquium on Ocean Hydrodynamics*, *34*, 13–73. https://doi.org/10.1016/S0422-9894(08)71237-6

Laurent, L. S., & Garrett, C. (2002). The role of internal tides in mixing the deep ocean. *Journal of Physical Oceanography*, *32*(10), 2882–2899. https://doi.org/10.1175/1520-0485(2002)032<2882:troiti>2.0.co;2

Lawrence, G. A. (1993). The hydraulics of steady two-layer flow over a fixed obstacle. *Journal of Fluid Mechanics*, *254*, 605–633. https://doi.org/10.1017/s0022112093002277

Macias, D., García, C. M., Navas, F. E., Váquez-López-Escobar, A., & Mejías, M. B. (2006). Tidal induced variability of mixing processes on Camarinal Sill (Strait of Gibraltar): A pulsating event. *Journal of Marine Systems*, *60*(1–2), 177–192. https://doi.org/10.1016/j.jmarsys.2005.12.003

Mauritzen, C., Morel, Y., & Paillet, J. (2001). On the influence of Mediterranean water on the central waters of the North Atlantic Ocean. *Deep-Sea Research I*, *48*(2), 347–381. https://doi.org/10.1016/s0967-0637(00)00043-1

Mercier, M. J., Gostiaux, L., Helfrich, K., Sommeria, J., Viboud, S., Didelle, H., et al. (2013). Large-scale, realistic laboratory modeling of M2 internal tide generation at the Luzon Strait. *Geophysical Research Letters*, *40*(21), 5704–5709. https://doi.org/10.1002/2013GL058064

Meteo France. (2023). Arpege model [Dataset]. Retrieved from https://donneespubliques.meteofrance.fr/?fond=produit&id_produit=130&id_rubrique=51

Morozov, E. G., Trulsen, K., Velarde, M. G., & Vlasenko, V. I. (2002). Internal tides in the Strait of Gibraltar. *Journal of Physical Oceanography*, *32*(11), 3193–3206. https://doi.org/10.1175/1520-0485(2002)032<3193:itits>2.0.co;2

Naranjo, C., García-Lajuente, J., Sannino, G., & Sanchez-Garrido, J. C. (2014). How much do tides affect the circulation of the Mediterranean Sea? From local processes in the Strait of Gibraltar to basin-scale effects. *Progress in Oceanography*, *127*, 108–116. https://doi.org/10.1016/j.pocean.2014.06.005

Navarro, G., Vicent, J., Caballero, I., Gómez-Enri, J., Morris, E. P., Sabater, N., et al. (2018). Improving the analysis of biogeochemical patterns associated with internal waves in the Strait of Gibraltar using remote sensing images. *Estuarine, Coastal and Shelf Science*, *204*, 1–13. https://doi.org/10.1016/j.ecss.2018.02.009

Özgökmen, T. M., Chassignet, E. P., & Rooth, C. G. H. (2001). On the connection between the Mediterranean outflow and the Azores current. *Journal of Physical Oceanography*, *31*(2), 461–480. https://doi.org/10.1175/1520-0485(2001)031<0461:otcbtm>2.0.co;2

Peliz, Á., Teles-Machado, A., Marchesiello, P., Dubert, J., & Garcia-Lafuente, J. (2009). Filament generation off the Strait of Gibraltar in response to gap winds. *Dynamics of Atmospheres and Oceans*, *46*(1), 36–45. https://doi.org/10.1016/j.dynatmoce.2008.08.002

Pratt, L. J. (2008). Critical conditions and composite Froude numbers for layered flow with transverse variations in velocity. *Journal of Fluid Mechanics*, *605*, 281–291. https://doi.org/10.1017/S002211200800150X

Pratt, L. J., Deese, H. E., Murray, S. P., & Johns, W. (2000). Continuous dynamical modes in straits having arbitrary cross sections, with applications to the Bab al Mandab. *Journal of Physical Oceanography*, *30*(10), 2515–2534. https://doi.org/10.1175/1520-0485(2000)030⟨2515:CDMISH⟩2.0.CO;2

Puertos del Estado (Spain). (2023). Tarifa tide gauge [Dataset]. Retrieved from http://opendap.puertos.es/thredds/catalog/tidegauge_tari/catalog.html

Rahmstorf, S. (1998). Influence of Mediterranean outflow on climate. *Eos, Transactions American Geophysical Union*, *79*(24), 281–282. https://doi.org/10.1029/98eo00208

Reid, J. L. (1979). On the contribution of the Mediterranean Sea outflow to the Norwegian-Greenland Sea. *Deep Sea Research Part A. Oceanographic Research Papers*, *26*(11), 1199–1223. https://doi.org/10.1016/0198-0149(79)90064-5

Richez, C. (1994). Airborne synthetic aperture radar tracking of internal waves in the Strait of Gibraltar. *Progress in Oceanography*, *33*(2), 93–159. https://doi.org/10.1016/0079-6611(94)90023-x

Sánchez-Garrido, J. C., Garcia-Lafuente, J., Aldeanueva, F. C., Baquerizo, A., & Sannino, G. (2008). Time-spatial variability observed in velocity of propagation of the internal bore in the Strait of Gibraltar. *Journal of Geophysical Research*, *113*(C7), C07034. https://doi.org/10.1029/2007jc004624

Sánchez-Garrido, J. C., & Nadal, I. (2022). The Alboran Sea circulation and its biological response: A review. *Frontiers in Marine Science*, *9*, 933390. https://doi.org/10.3389/fmars.2022.933390

Sánchez-Garrido, J. C., Sannino, G., Liberti, L., García-Lafuente, J., & Pratt, L. (2011). Numerical modeling of three-dimensional stratified tidal flow over Camarinal Sill, Strait of Gibraltar. *Journal of Geophysical Research*, *116*(C12), C12026. https://doi.org/10.1029/2011jc007093

Sannino, G., Bargagli, A., & Artale, V. (2002). Numerical study of the hydraulics of the mean flow through the Strait of Gibraltar.

Sannino, G., Bargagli, A., & Artale, V. (2004). Numerical modeling of the semidiurnal tidal exchange through the Strait of Gibraltar. *Journal of Geophysical Research*, *109*(C5), C05011. https://doi.org/10.1029/2003JC002057

Sannino, G., Carillo, A., & Artale, V. (2007). Three-layer view of transports and hydraulics in the Strait of Gibraltar: A three-dimensional model study. *Journal of Geophysical Research*, *112*(C3), C03010. https://doi.org/10.1029/2006JC003717

Sannino, G., Carillo, A., Pisacane, G., & Naranjo, C. (2015). On the relevance of tidal forcing in modelling the Mediterranean thermohaline circulation. *Progress in Oceanography*, *134*, 304–329. https://doi.org/10.1016/j.pocean.2015.03.002

Shroyer, E., Moum, J., & Nash, J. (2009). Observation of polarity reversal in shoaling nonlinear internal waves. *Journal of Physical Oceanaography*, *39*(3), 691–701. https://doi.org/10.1175/2008jpo3953.1

Vargas, J. (2004). *Fluctuaciones subinerciales y estado hidráulico del intercambio a través del Estrecho de Gibraltar*. Ph.D. thesis, Universidad de Sevilla.

Vargas, J., García-Lafuente, J., Candela, J., & Sánchez, A. J. (2006). Fortnightly and monthly variability of the exchange through the Strait of Gibraltar. *Progress in Oceanography*, *70*(2–4), 466–485. https://doi.org/10.1016/j.pocean.2006.07.001

Vásquez, A., Bruno, M., Izquierdo, A., Macías, D., & Cañavate, A. R. (2008). Meteorologically forced subinertial flows and internal wave generation at the main sill of the Strait of Gibraltar. *Deep-Sea Research I*, *55*(10), 1277–1283. https://doi.org/10.1016/j.dsr.2008.05.008

Vásquez, A., Stashchuk, N., Vlasenko, V., Bruno, M., Izquierdo, A., & Gallacher, P. C. (2006). Evidence of multimodal structure of the baroclinic tide in the Strait of Gibraltar. *Geophysical Research Letters*, *33*(17), L17605. https://doi.org/10.1029/2006gl026806

Violette, P. L., & Lacombe, H. (1988). Tidal-induced pulses in the flow through the Strait of Gibraltar. *Oceanology Acta, SP*, 13–17.

Vlasenko, V., Garrido, J. C. S., Stashchuk, N., Lafuente, J. G., & Losada, M. (2009). Three-dimensional evolution of large-amplitude internal waves in the Strait of Gibraltar. *Journal of Physical Oceanography*, *39*(9), 2230–2246. https://doi.org/10.1175/2009JPO4007.1

Volkov, D. L., & Fu, L.-L. (2010). On the reasons for the formation and variability of the Azores Current. *Journal of Physical Oceanography*, *40*(10), 2197–2220. https://doi.org/10.1175/2010jpo4326.1

Watson, G., & Robinson, I. (1990). A study of internal wave propagation in the Strait of Gibraltar using shore-based marine radar images. *Journal of Physical Oceanography*, *20*(3), 374–395. https://doi.org/10.1175/1520-0485(1990)020<0374:asoiwp>2.0.co;2

Wesson, J. C., & Gregg, M. (1994). Mixing at Camarinall Sill in the Strait of Gibraltar. *Journal of Geophysical Research*, *99*(C5), 9847–9878. https://doi.org/10.1029/94jc00256

Ziegenbein, J. (1969). Short internal waves in the Strait of Gibraltar. *Deep-Sea Reasearch*, *16*(5), 479–487. https://doi.org/10.1016/0011-7471(69)90036-9

Ziegenbein, J. (1970). Spatial observations of short internal waves in the Strait of Gibraltar. *Deep-Sea Reasearch*, *17*(5), 867–875. https://doi.org/10.1016/0011-7471(70)90004-5